High b-value Diffusion MRI for Characterizing White Matter Damage

BY

Jin Gao
B.S., Inner Mongolia Agricultural University, China, 2011

THESIS

Submitted as partial fulfillment of the requirements
for the degree of Master of Science in Bioengineering
in the Graduate College of the
University of Illinois at Chicago, 2017

Chicago, Illinois

Defense Committee:

Richard L. Magin, Ph.D., Chair and Advisor
Weiguo Li, Ph.D., Research Resources Center, UIC
Kejia Cai, Ph.D., Department of Radiology, UIC

This thesis is dedicated to my parents for their unconditional love and continuous support.

ACKNOWLEDGEMENTS

CONTRIBUTION OF AUTHORS

Chapter 1 is an introduction including the background, motivation and objectives of my thesis. Chapter 2 reviews the basics of MRI. Chapter 3 reviews diffusion MRI. Chapter 4 represents my unpublished work that I was the major driver of the research. Dr. Rodolfo Gatto assisted me in sample preparation and histology results shown in Fig 4-14. Steven D. Price assisted me in histology results shown in Fig 4-14. Chapter 5 represents my overarching conclusions and future research directions.

TABLE OF CONTENTS

LIST OF TABLES

LIST OF FIGURES

LIST OF ABBREVIATIONS

ALS	Amyotrophic Lateral Sclerosis
CNR	Contrast-to-noise Ratio
CST	Corticospinal Tract
CTRW	Continuous-time Random Walk
DTI	Diffusion Tensor Imaging
DWI	Diffusion Weighted Imaging
ETL	Echo Train Length
EPI	Echo Planar Imaging
FID	Free Induction Decay
fMRI	Functional Magnetic Resonance Imaging
FOV	Field of View
FROC	Fractional Order Calculus
GM	Gray Matter
IVIM	Intravoxel Incoherent Motion Imaging
MD	Mean Diffusivity
MR	Magnetic Resonance
MRI	Magnetic Resonance Imaging
NMR	Nuclear Magnetic Resonance
RF	Radio-frequency
ROI	Regions of Interest
SC	Spinal Cord
SNR	Signal-to-Noise Ratio

SOD1	Superoxide Dismutase 1
STEAM	Stimulated Echo Acquisition Mode
T_1	Spin-lattice Relaxation
T_2	Spin-spin Relaxation
TE	Echo Time
TR	Repetition Time
WM	White Matter
WT	Wild Type

SUMMARY

Diffusion magnetic resonance imaging has been widely used to study white matter diseases due to the ubiquity and its non-invasive nature. Amyotrophic lateral sclerosis (ALS), characterized with white matter track damage, is a progressive motor neuron disease in brain and spinal cord with an unknown etiology. Most of diffusion MRI studies focused on altered water diffusion properties in white mater. Nevertheless, Irena Niebroj-Dobosz and coworkers associated this disease with myelin changes [1]. Thus, the white matter damage might be reflected by the changes of myelin diffusion behaviors that are highly critical, but rarely studied. Furthermore, diffusion MRI studies on spinal cord, the typical onset area in ALS, can play an important role in assessing the disease progression, revealing etiology and monitoring treatments.

This thesis aims to characterize white matter damage in a murine model of ALS by analyzing the diffusion properties of myelin using ultra high b-value (up to 8.58×10^5 s/mm^2) diffusion MRI. All MRI measurements were performed using a 9.4 T MRI scanner (Agilent, Santa Clara, CA). Stimulated echo acquisition mode sequence was employed with diffusion gradients applied in parallel and perpendicular to the long axis of spinal cord of symptomatic G93A-SOD1 and wild type animal groups respectively. Fast spin echo sequence was employed for anatomical images (T$_2$ weighted). Three diffusion models, bi-exponential, continuous-time random walk (CTRW) model and bi-component model combining CTRW and mono-exponential models were used to analyze the data. Axonal fiber morphology and integrity of the spinal cords were validated by histological analysis. We found differences of signal intensities at lumbar level between diseased and control animals and diffusion-weighted signal decay varied with the diffusion weighting direction relative to spinal nerve fiber orientation on high b-value diffusion-

weighted images. Additionally, we found the bi-component model demonstrated the best fit among the three models.

In summary, this work has demonstrated the feasibility of diffusion MRI at high b values to evaluate spinal cord alterations in a symptomatic mouse model of ALS. In addition, high b-value diffusion MRI has potential to evaluate spinal cord alterations in other diseases associated with white matter damage. Further studies of building new models to differentiate the progression of disease are needed.

1. INTRODUCTION

1.1 BACKGROUND

Since the first images were acquired by Paul Lauterbur in 1973, magnetic resonance imaging (MRI) has been well developed and applied widely in clinical diagnosis [2]. Although it was developed most recently compared with X-ray/CT, Nuclear Medicine and Ultrasound, MRI has become one of the safest and most common imaging modalities since it has good soft tissue contrasts, a noninvasive nature and multi-planar visualization of whole body [2]. By 2010, approximately 30 million MRI scans were done world widely by tens of thousands of researchers and radiologists, and the annual number of publication regarding to nuclear magnetic resonance (NMR) and MRI increased to 35,000 [3]. Nowadays it has various contrast mechanisms, such as proton density, spin-lattice relaxation (T_1), spin-spin relaxation (T_2), chemical exchange saturation transfer (CEST), magnetic resonance elastography (MRE) and diffusion MRI. Diffusion MRI is one of the most important and widely used technologies. It uses the Brownian motion of water molecules as a probe to detect the microstructure of biological tissues. More and more models and methods based on diffusion MRI are developed and studied, for example, mono-exponential model, bi-exponential model, fractional order calculus (FROC) model, continuous-time random walk (CTRW) model, intravoxel incoherent motion imaging (IVIM), diffusion tensor imaging (DTI), diffusion kurtosis imaging (DKI), and diffusion spectrum magnetic resonance imaging (DSI).

1.2 MOTIVATION

For most of diffusion MRI applications, b value, a factor decided by diffusion time, strength and duration of gradients, is less than 6000 s/mm^2. This limits the diffusion MRI studies

on water diffusion behaviors. Nevertheless, in the diseases associated with white matter damage, altered myelin diffusion properties can directly reflect changes in spinal cord. The overall goal of this study is to investigate the feasibility of high b-value diffusion MRI to evaluate white matter damage in spinal cord.

1.3 THESIS OBJECTIVES

To meet the overall goal, the study includes three specific aims:

Specific aim 1 To investigate the differences of signal intensities between control and diseased animals of ALS in diffusion weighted images at high b values.

Specific aim 2 To develop a diffusion model to describe the diffusion properties of myelin and changes at white matter track damages from the data acquired at multiple b values.

Specific aim 3 To apply the developed diffusion models for differentiating and quantifying the white matter changes in a murine model of ALS.

2. MAGNETIC RESONANCE IMAGING

MRI is an image technology based on nuclear magnetic resonance (NMR) phenomenon that was discovered by Isidor Rabi in 1938 and the spatial information encoding developed by Paul Lauterbur in 1973, MRI [4]. Compared with other imaging modalities, MRI can obtain not only multidimensional images, but also 2D and 3D images at any orientation. Like positron emission tomography and single-photon emission computed tomography, MRI is a form of emission tomography, which means MR signals were directly collected from the object itself [4]. However, there is no need to inject radioactive isotopes into the object to generate MRI signals [4]. Moreover, excitations of NMR phenomenon are at radio-frequency (RF) range, which means there is no ionizing radiation during the acquirement [4]. Thus, MRI is known as a safe imaging modality with no nonradioactive risk and ionizing radiation.

2.1 FOUNDAMENTALS OF NMR

2.1.1 Nuclear Magnetic Moment

It's a good start to understand NMR phenomenon with Felix Bloch's theory that a spinning charged particle, like any spinning charged object, creates an electromagnetic field, which is as similar as surrounding a microscopic magnetic bar [4, 5]. Physically, a spinning charged particle can be regarded as a vector $\vec{\mu}$, known as nuclear magnetic dipole moment or magnetic moment [4].

Multiple nuclei (charged particles) can be used for MRI, such as proton (^{1}H), ^{13}C, ^{19}F and ^{31}P. Also, there are multiple nuclei cannot be used for MRI, such as ^{12}C, ^{16}O, and ^{32}S. Proton is the most commonly used nuclei due to its abundancy in body.

2.1.2 Nuclei in Magnetic Field

Since the magnetic moment $\vec{\mu}$ is a vector, it has both magnitude and orientation. The magnitude is fixed for a certain condition. The orientation is completely random if there is no external magnetic field due to thermal random motion, as shown in Fig 2-1 (A). Nevertheless, when there is an external magnetic field (B_0), the magnetic moment $\vec{\mu}$ will point at two orientations, parallel with or antiparallel with the external magnetic field, as shown in Fig 2-1 (B).

(A)   (B)
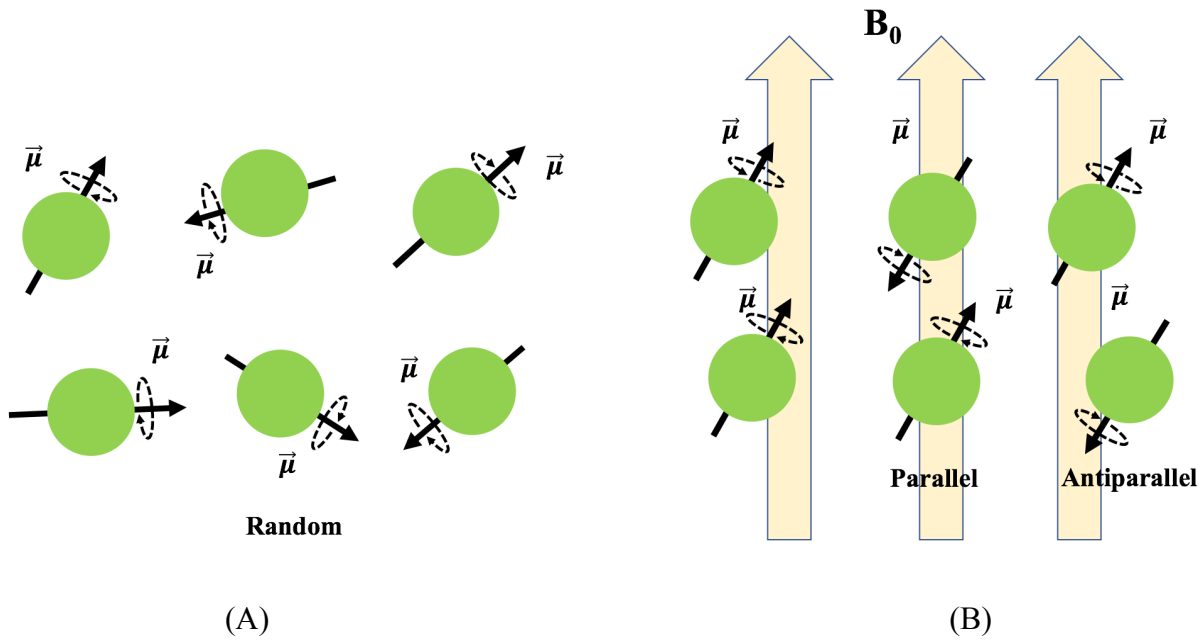
Figure 2 - 1 spinning charged particles, (A) the magnetic moment μ pointing randomly and (B) the magnetic moment μ pointing parallel with or antiparallel with the external magnetic field.

The number of protons in parallel state or in antiparallel state is depended on B_0 value, type of nuclei and temperature:

$$\frac{N_{antiparallel}}{N_{parallel}} = 1 - \left[\frac{\gamma h B_0}{2\pi k T}\right] \qquad (2\text{-}1)$$

where γ is gyromagnetic ratio, h is Planck's constant (6.63 x 10^{-34} J s), k is Boltzmann's constant (1.38 x 10^{-23} J/K) and T is the temperature in Kelvin [2]. The difference between $N_{parallel}$ and $N_{antiparallel}$ can be denoted as:

$$N_{parallel} - N_{antiparallel} = N_{total} \cdot \frac{\gamma h B_0}{4\pi kT} \qquad (2\text{-}2)$$

Although the protons in parallel state are more energy 'favorable' than them in antiparallel state, the difference between them is trivial [2]. For instant, in 1.5 T magnet and room temperature 300K the difference rate is 5.114×10^{-6}, as shown in Eq 2-3, which means that there are approximately five in a million protons for generating MR signals. Thus, NMR has a low-sensitivity.

$$\frac{N_{parallel} - N_{antiparallel}}{N_{total}} = \frac{\gamma h B_0}{4\pi kT} = \frac{\frac{\gamma}{2\pi} h B_0}{2kT} = \frac{42.58 \times 10^6 Hz/T \times 6.63 \times 10^{-34} \, J \cdot s \times 1.5 \, T}{2 \times 300K \times 1.38 \times 10^{-23} \, J/K} = 5.114 \times 10^{-6} \quad (2\text{-}3)$$

Furthermore, with an external magnetic field (B_0), protons will not only point at two orientations, but also doing circular motions around z-axis with a certain angle. Nuclear precession is introduced to describe these motions, as shown in Fig 2-2.
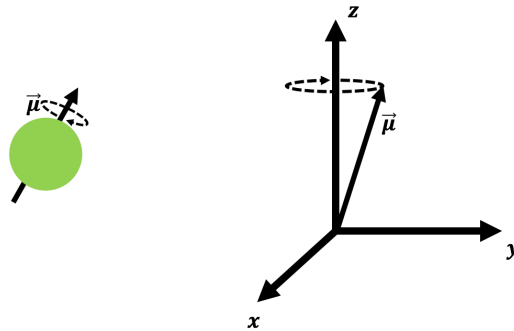
Figure 2 - 2 Precession of a nuclear spin in an external magnetic field is similar to a circular motion around z-axis.

To specify precession, angular frequency and left-hand rule are used. Angular frequency of nuclear precession is defined as:

$$\omega_0 = \gamma B_0 \tag{2-4}$$

which is also known as Larmor frequency. The left-hand rule is used to decide precession direction. That is, put the left thumb point along B_0 direction and the other four fingers show the precession direction [4].

2.1.3 Net Magnetization

To describe all protons in an object, net magnetization defined as the sum of all the individual magnetic moments $\vec{\mu}$ is introduced:

$$\vec{M} = \sum_{n=1}^{N} \vec{\mu}_n \tag{2-5}$$

where N is the total number of protons [4]. Also, the net magnetization $\vec{M}$ points along B_0 direction. Moreover, there is zero transverse component of net magnetization due to random phases of precession of single magnetic moment, although the transverse component exists for each magnetic moment due to the certain angle of precession [4].

2.1.4 RF Excitation

In system that all spins process around B_0 field, if an oscillating magnetic field $\vec{B}_1(t)$ is applied with the same frequency as precessing spins, the energy of $\vec{B}_1(t)$ will be absorbed. This external energy should be equal to the difference between these two states:

$$E_{rf} = \Delta E = \gamma \hbar B_0 \tag{2-6}$$

Since the energy that carries by electromagnetic radiation at frequency (ω_{rf}) is defined as:

$$E_{rf} = \hbar \omega_{rf} \tag{2-7}$$

, when the frequency (ω_{rf}) of electromagnetic radiation at frequency equals to frequency of spin precession (ω_0)

$$\omega_{rf} = \omega_0 \tag{2-8}$$

a coherent transition will be induced, which is known as the resonance condition.

The $B_1(t)$ field can be denoted as RF pulse due to its short turn-on time, normally a few microseconds or milliseconds [4]. Also, the strength of this field is much smaller than B_0 field, normally dozens of Gauss. The $B_1(t)$ field is consisted of a pulse envelope function and excitation carrier frequency:

$$\vec{B}_1(t) = 2B_1{}^e(t)\cos{(\omega_{rf}t + \varphi)}\vec{v} \tag{2-9}$$

where $B_1{}^e(t)$ is the pulse envelope function, ω_{rf} is the excitation carrier frequency, φ is the initial angle and $\vec{v}$ is the direction that $B_1(t)$ field is added [4]. The envelope function $B_1{}^e(t)$ is vital to RF pulse because it is decided the shape and duration, which means its excitation properties [4]. For instant, short rectangular pulses, as known as hard pulse, can excite a wide range frequency in the spin system. On the other hand, pulses with long bandwidth are often called soft pulses because they only excite a narrow band of frequencies.

2.1.5 Rotating Frame of Reference

To simplify modeling the precession, a new frame rotated simultaneously with precession at Larmor frequency ω_0 is introduced [5]. Within the rotating frame, object precessing at ω_0 remains stationary as shown in Fig 2-3 (A) (B) [2]. When a $B_1(t)$ field applied, it looks like a simple arc from z-axis into x-y plane within the rotating frame, as shown in Fig 2-3 (C) [5]. Comparing to the orthogonal axes x, y and z in laboratory frame, x', y' and z' has been used to denote the orthogonal axe in rotating frame. The corresponding unit vectors in rotating frame are $\vec{i'}$, $\vec{j'}$ and $\vec{k'}$, which are defined as

$$\vec{i'} = \cos(\omega t)\,\vec{i} - \sin{(\omega t)}\vec{j}$$

$$\vec{j'} = \sin(\omega t)\,\vec{i} + \cos{(\omega t)}\vec{j}$$

$$\vec{k'} = \vec{k} \tag{2-10}$$

where $\vec{i}$, $\vec{j}$ and $\vec{k}$ are the unit vector in laboratory frame and ω is the rotating frequency. When $\omega = \omega_0$, the rotating frame is called Larmor-rotating frame. When $\omega = \omega_{rf}$, the rotating frame is called RF-rotating frame. When $\omega_{rf} = \omega_0$, they are same.

(A)   (B)   (C)
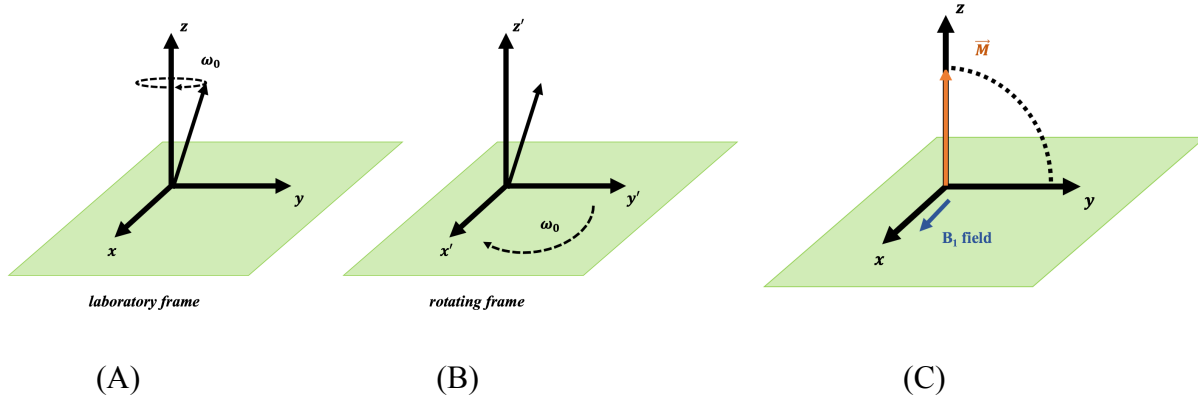
Figure 2 - 3 Rotating frame, (A) a vector precesses at frequency ω_0 in laboratory frame, (B) a vector precesses at frequency ω_0 in rotating frame at the same frequency and (C) simple arc visualized in rotating frame.

2.1.6 T_1 and T_2 Relaxation

If the $\vec{B}_1(t)$ field is applied on a spin system in B_0 field, the net magnetization $\vec{M}$ will be like a vector precessing around $\vec{B}_1(t)$ in rotating frame. The angular frequency ω_1 of the precession is defined as

$$\omega_1 = \gamma B_1 \qquad (2\text{-}11)$$

Normally, the precession around $\vec{B}_1(t)$ is unnecessary but a desired flip angle α is needed. The flip angle is defined as

$$\alpha = \omega_1 \tau = \gamma B_1 \tau \qquad (2\text{-}12)$$

where τ is RF excitation duration. Commonly, the RF pulse that can flip $\vec{M}$ from z'-axis to y'-axis in rotating frame by α angle are called α pulse, such as 90° or $\frac{\pi}{2}$ pulse rotated $\vec{M}$ by 90°.

Since excited state is not a favorite state, the spin system will return to ground state after an α pulse by emitting RF waves that carries the extra energy. The phenomenon of returning to ground state is known as relaxation. Also, the relaxation can be separated into two independent processes regarding to z axis component and x-y plane component respectively. T_1-relaxation, also called spin-lattice relaxation, indicates z axis component recovery and T_2-relaxation, also known as spin-spin relaxation, indicated x-y plane component decay. T_1 and T_2 are used to denote the time for the two relaxation processes respectively. Generally, T_1 is much longer than T_2 and different tissues have various T_1s and T_2s as shown in Table 2.1 [2].

Table 2. 1 Tissue relaxation time at 3T

	Brain (White Matter)	Brain (Gray Matter)	Liver	Skeletal Muscle	Lipid (Subcutaneous)	Cartilage
T_1 (ms)	1100	1600	800	1420	360	1240
T_2 (ms)	60	80	40	30	130	37

2.1.7 Free Induction Decay

The x-y plane component of net magnetization ($\vec{M}_{xy}$) is decaying over T_2 relaxation. This decay causes a time-variant coherent magnetic field that can induce an electric and magnetic field (emf) in coils wrapped up on the x-axis and y-axis [6]. This is known as Free Induction Decay (FID). The emf in coils are recorded as FID signals which is primary NMR signals. To maximize the signals, $\frac{\pi}{2}$ pulse is optimum because it tips $\vec{M}$ down into x-y plane where the $\vec{M}_{xy}$ is the maximum.

2.2 PRINCIPLES OF MRI

The NMR signals are contributed from an entire subject. To generate an image, a spatial encoding is needed. In 1973, Paul Lauterbur acquired the first images by employing three linear magnetic field gradient coils to encode spatial information in spins [7].

2.2.1 Magnetic Field Gradient

Three sets of magnetic field gradients are required in MR image acquisition: slice-selective gradient, frequency-encoding gradient and phase-encoding gradient [4].

The slice-selective gradient, as the name implied, is used with RF excitation to excite a certain slice of spins. Specifically, linear magnetic field gradient coils generate a gradient in B_0 field along a certain direction [4]. According to the definition of Larmor frequency, Equation (2-4), the angular frequency of nuclear precession becomes

$$\omega(z) = \gamma(B_0 + G_{ss}(t) \cdot z) = \omega_0 + \gamma \cdot G_{ss}(t) \cdot z \qquad (2\text{-}13)$$

where $G_{ss}(t)$ is a time-dependent function of gradient and z is the position along a certain direction [4]. For instance, if the position is in the center of the gradient, $z = 0$ and the $\omega(z)$ will equal to ω_0. If the position is at the edge, z will be positive or negative maximum and $\omega(z)$ will not equal to ω_0 but have the maximum difference of $\gamma \cdot G_{ss}(t) \cdot z$. Therefore, the spatial information along the certain direction is encoded in $\omega(z)$. Correspondingly, the RF excitation frequency ω_{rf} changes with positions, which means a certain ω_{rf} will excite only a certain slice instead of the entire subject.

Similarly, frequency-encoded gradient uses the gradient $G_{fe}(t)$ to encode spatial information along a certain direction in the slice that selected by the gradient $G_{ss}(t)$. The Larmor frequency at position x is

$$\omega(x) = \omega_0 + \gamma \cdot G_{fe}(t) \cdot x \qquad (2\text{-}14)$$

Unlike the slice-selective gradient, frequency-encoded gradient encodes the spatial information along x into the FID signal $S(t)$, as shown in

$$S(t) = \left[\int_{-\infty}^{\infty} \rho(x) e^{-i\gamma \cdot G_{fe}(t) \cdot x \cdot t} \, dx \right] \cdot e^{-iw_0 t} \qquad (2\text{-}15)$$

where $\rho(x)$ is the proton density in slice [4]. After removing carrier frequency $e^{-iw_0 t}$, Equation (2-15) is rewritten as

$$S(t) = \int_{-\infty}^{\infty} \rho(x) e^{-i\gamma \cdot G_{fe}(t) \cdot x \cdot t} \, dx \qquad (2\text{-}16)$$

The gradient $G_{fe}(t)$ makes local spins out of phase coherence, which means the signal with the gradient $G_{fe}(t)$ decays faster than them without a gradient [4].

Same as frequency-encoded gradient, phase-encoded gradient encodes spatial information along y into the FID signal $S(t)$, as shown in [4]

$$S(t) = \left[\int_{-\infty}^{\infty} \rho(y) e^{-i\gamma \cdot G_{pe}(t) \cdot y \cdot \tau_{pe}} \, dy \right] \cdot e^{-iw_0 t} \qquad (2\text{-}17)$$

Also, carrier frequency $e^{-iw_0 t}$ can be removed and Equation (2-17) is rewritten as

$$S(t) = \int_{-\infty}^{\infty} \rho(y) e^{-i\gamma \cdot G_{pe}(t) \cdot x \cdot \tau_{pe}} \, dy \qquad (2\text{-}18)$$

where τ_{pe} is the duration of frequency-encoded gradient turned on. Since spins dephase with the gradient turned on for a certain time, the spins will have different phases if gradient is turned off. The various phases carry spatial information along phase direction and are recorded by coils [4].

2.2.2 The k-space

k-space is a data space where the measured MRI signals are stored. The values in k-space are spatial frequencies, which can be described as

$$S(k_x, k_y) \propto \iint_{slice} \rho(x, y) e^{-i2\pi k_x x} e^{-i2\pi k_y y} \, dx \, dy \qquad (2\text{-}19)$$

where k_x and k_y are defined as [2]

$$k_x = \frac{\gamma}{2\pi} G_x t$$

$$k_y = \frac{\gamma}{2\pi} G_y \tau_{pe} \qquad (2\text{-}20)$$

Multiple trajectories are used to fill these signals in k-space, such as Cartesian raster, radial, zigzag and spiral [8]. There is no perfect trajectory. Instead, each trajectory has its own advantages and disadvantages. Selection of a desired trajectory depends on the sequence and application. For instance, echo planar imaging (EPI) is used commonly in functional MRI (fMRI) and zigzag trajectory is employed due to the its fast speed. Generally, Cartesian raster is the most popular used one due to less artifacts. In this case, all lines are paralleled and each of them is corresponded to a readout on a certain initial phase.

2.2.3 Image Contrast

Signal-to-noise ratio (SNR) is critical for image contrast because it describes the relative contributions of true signals and noise [9]. High SNR, therefore, is always desired. The most commonly used SNR calculation is

$$SNR = \frac{S}{\sigma_{noise}} \qquad (2\text{-}21)$$

where S is signal intensity of a pixel, σ_{noise} is the standard deviation of background [2].

Generally, there are several factors affected SNR,

$$SNR \propto \left(\frac{FOV_x}{N_x} \cdot \frac{FOV_y}{N_y} \cdot \Delta z \right) \cdot \sqrt{\frac{N_x \cdot N_y \cdot NEX}{BW}} \qquad (2\text{-}22)$$

where FOV_x and FOV_y are the field of view of frequency-encoding and phase encoding direction, N_x and N_y are the numbers of frequency-encoding and phase encoding steps, NEX is the number of excitations, BW is full bandwidth and Δz is slice thickness. Thus, a desirable SNR can be acquired by optimizing the parameters in Equation (2-22).

Contrast-to-noise ratio is another crucial concept that need to be considered, defined as

$$CNR = \frac{C_{AB}}{\sigma_{noise}} = \frac{|S_A - S_B|}{\sigma_{noise}} = |SNR_A - SNR_B| \qquad (2\text{-}23)$$

where C_{AB} is the image contrast, S_A is the intensity of tissue A, S_B is the intensity of tissue B and σ_{noise} is the standard deviation of background [2]. So, CNR is depended on both SNR and spatial resolution that is related to the smallest distance between two features [2]. High CNR is also desired. There are multiple ways to generate MRI contrast, such as T_1, T_2, blood oxygen level- dependent, chemical exchange, and diffusion.

3. DIFFUSION MAGNETIC RESONANCE IMAGING

In MRI, diffusion as a contrast mechanism is mainly based on the Brownian motion of water molecules. For example, when ink drops into a cup of water for a couple of seconds, the center of the ink droplet remains the same position but its sphere shape gets bigger due to Brownian motion of water molecules, which is known as isotropic diffusion as shown in Fig 3-1 (A). If there are some micron scaffolds in the water, the droplet shape will not be sphere due to the restrictions from the scaffolds. Instead, the shape will be ellipsoid whose long axis is along the fiber direction of the scaffolds, which is known as anisotropic diffusion as shown in Fig 3-1 (B).

(A)   (B)
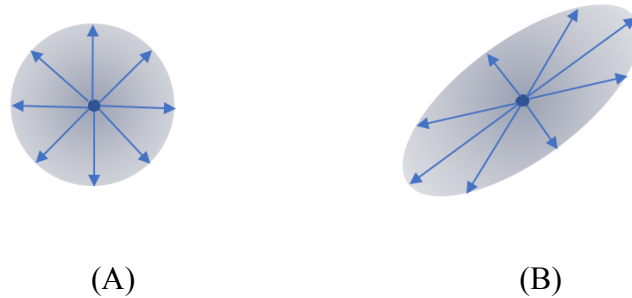
Figure 3 - 1 Water molecules diffusion, (A) isotropic diffusion and (B) anisotropic diffusion.

Diffusion carries information of micro environment of molecules. That is, the diffusion diameter will be larger with less restricted environment, and vice versa. Also, diffusion along several certain orientations (at least 6 directions) can show a fiber track map.

There are other water motions affected MRI, bulk motion of water molecules and flow. The former describes the water moved with an entire object movement. It will cause several artifacts, such as image blurring and ghosting. The latter defines the case that the center of diffusion moves with time without an entire object movement. In high speed flow, such as large arteries, the water molecules that have been excited are flushed away from the excited slice. So,

no signal will be acquired, which doesn't affect diffusion measurements for the slice. In a slow speed flow that the excited water molecules stay in the slice and diffusion of them is slow enough, the water molecules motion is depended on both flow and diffusion, which is known as perfusion. When diffusion of the excited water molecules is large enough, flow doesn't affect the water molecules motion, which means only diffusion is considered for the motion.

3.1 BASICS OF DIFFUSION MRI

Although diffusion MRI is known as a family of techniques including diffusion weighted imaging (DWI), diffusion tensor imaging (DTI), quantitative mapping of diffusion coefficients, DWI is the basis of other techniques. To acquire diffusion weighted images, a diffusion-weighting gradient pulse is employed. It consists of a pair of gradients to dephase and rephase spins in a certain orientation. The dephasing gradient introduces a phase difference $\varphi(x)$ along this direction, as illustrated in

$$\varphi(x) = e^{i\gamma G_{df}\delta x} \tag{3-1}$$

where x is the distance, G_{df} is diffusion-weighting gradient strength and δ is applied duration, also as known as pulse width. During a time interval Δ, as known as diffusion time, spins diffused. The population of diffused water molecules at location x at the time point t is defined as

$$P(x,t) = \frac{1}{\sigma\sqrt{2\pi}} e^{-x^2/2\sigma^2} \tag{3-2}$$

where σ is the mean diffusion distance that is defined by Einstein's equation as

$$\sigma = \sqrt{2D\Delta} \tag{3-3}$$

where D is diffusion constant. Substituting Equation (3-3) into Equation (3-2), the population is

$$P(x,t) = \frac{1}{\sqrt{4\pi Dt}} e^{-x^2/4Dt} \tag{3-4}$$

15

Since the rephasing gradient refocuses the stationary spins, the signal S' from diffused water molecules is defined as

$$S' = \int_x P(x,t) \cdot \varphi(x)dx = \int_x \frac{1}{\sqrt{4\pi Dt}} e^{-x^2/4Dt} \cdot e^{i\gamma G_{df}\delta x}dx = e^{-\gamma^2 G_{df}^2 \delta^2 D\Delta} \quad (3\text{-}5)$$

After simplification, Equation (3-5) is rewritten as

$$S' = e^{-\gamma^2 G_{df}^2 \delta^2 D\Delta} \quad (3\text{-}6)$$

Since S' is normalized but the acquired signals have intensities, the signal S with diffusion gradient is defines as

$$S = S_0 \cdot S' = S_0 \cdot e^{-\gamma^2 G_{df}^2 \delta^2 D\Delta} \quad (3\text{-}7)$$

where S_0 is the signal without a diffusion-weighting gradient. Equation (3-7) is built on an assumption that pulse width (δ) is small enough to be neglected. However, in practical, it is relative long (5-30ms) regarding to molecule diffusion, which means it has to be considered [10]. Therefore, the signal S is redefined as

$$S = S_0 \cdot e^{-\gamma^2 G_{df}^2 \delta^2 \left(\Delta - \delta/3\right)D} \quad (3\text{-}8)$$

To simplify Equation (3-8), b is defined as

$$b = \gamma^2 G_{df}^2 \delta^2 \left(\Delta - \delta/3\right) \quad (3\text{-}9)$$

Thus, the signal S can be written as

$$S = S_0 \cdot e^{-bD} \quad (3\text{-}10)$$

The unit for b calculated from Equation (3-9) is s/mm^2. Since b and D are reciprocals, the unit of D is mm^2/s. The apparent diffusion coefficient (ADC) values of tissues at 1.5 T are shown in Table 3.1 [11, 12].

Table 3. 1 Apparent diffusion coefficients (ADCs) within tissues at 1.5 T

	Brain (Cortical Gray Matter)	Brain (Deep Gray Matter)	Brain (White Matter)	Liver	Kidney	Pancreas
ADC ($\times 10^{-3}$mm2/s)	0.78-1.09	0.64-0.83	0.62-0.79	1.4-1.8	1.8-2.2	1.08-2.65

Only the spins along diffusion-weighting gradient G_{df} are dephased, so the diffusion along G_{df} is measured. That is, the gradient orientation decides the diffusion direction that is measured. In most cases, the orientation is arbitrary. Nevertheless, the orientation matters in some studies, for example, DTI and high b diffusion in spinal cord in this study.

3.2 DIFFUSION OF MACROMOLECULES

Besides water diffusion, small and large size molecule diffusion can be used as probes to study the metabolisms that they take part in. For instance, lipids become a hot topic because they are metabolic active and play very important roles in obesity and diabetes [13]. Since diffusion of lipid is decided by molecular weight, droplet size, temperature and microenvironment, the diffusion properties reflect the differences in tissues [14, 15]. Moreover, the diffusion behaviors of lipid are largely different from water diffusion because lipids have lower diffusivities due to large molecule weights and more restricted environments [15]. Therefore, lipid diffusion behaviors can be studied at a very high b value that most of water diffusion signals are decayed away.

3.3 DIFFUSION MRI PULSE SEQUENCES

Since a diffusion-weighting gradient can be incorporated into any kind of pulse sequence, plenty of the combinations are used, such as spin echo, fast spin echo, single-shot echo planar imaging (EPI), stimulated echo acquisition mode (STEAM), steady-state free precession (SSFP), and gradient and spin echo (GRASE) diffusion-weighing pulse sequence [8]. Generally, the spin echo sequence with appropriate gating for respiration/electrocardiograph (ECG) or a navigator echo provides high-quality diffusion weighted images with minimum artifacts [8]. Nevertheless, it is not common used due to a long acquisition time. Instead, fast spin echo and EPI based diffusion-weighting pulse sequence are popular. However, both of them have their own disadvantages, such as reduced SNR due to large effective echo time (TE) in a long echo train length (ETL) that inherited from fast spin echo and enhanced eddy current artifacts due to system imperfection in single-shot EPI.

STEAM incorporating diffusion-weighting gradient is common used in high b-value diffusion, in ex vivo studies and in tissue with short T_2 due to relatively long time τ_m for molecules diffusion, as shown in Fig 3-2 [16, 17].
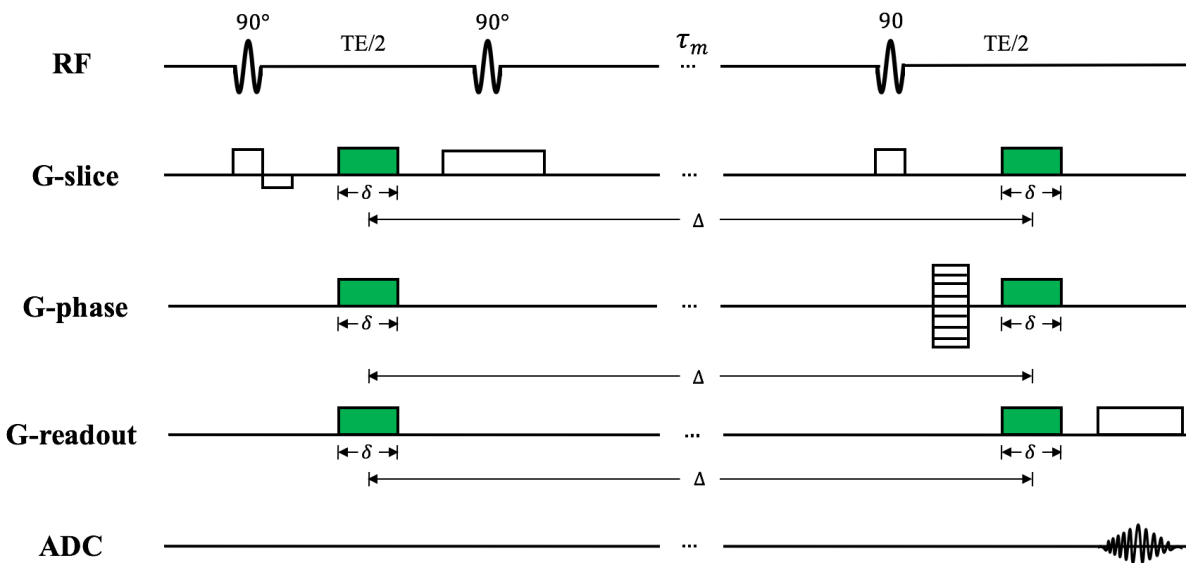
Figure 3 - 2 A diagram of STEAM based diffusion-weighting pulse sequence.

Specially, a high b-value can be achieved by large diffusion gradient strength G_{df}, pulse width δ and diffusion time Δ, as illustrated in Equation (3-9). The first two variables are hard to be large enough to meet requirement due to hardware limitations and short TE. The diffusion time Δ, therefore, becomes a desirable variable to increase the b-value. However, the popular diffusion-weighting pulse sequences based on fast spin echo and EPI cannot achieve a long diffusion time, since they are depended on T_2 or $T_2{}^*$ decay. Instead, τ_m in STEAM sequence that is depended on T_1 relaxation enables long diffusion time [18]. Therefore, STEAM sequence is suitable for tissues with short T2 [16]. Yet, STEAM based diffusion-weighting pulse sequence has some disadvantages. For example, it is the trivial in spin echo based diffusion sequence that a crusher before slice gradient contributes to dephasing as same as a diffusion gradient, but unneglectable in STEAM based diffusion sequence due to long diffusion time. According to the definition of b-value, as illustrated in Equation (3-9), the small difference between b values calculated by G_{df} and G_{df}' that considers the contribution of the crusher is enlarged by multiplying a larger diffusion time Δ.

3.3 DIFFUSION MRI MODELS

As mentioned in section 3.1, quantitative mapping of diffusion coefficients is one of the diffusion MRI techniques to analyze diffusion properties. A Gaussian or non-Gaussian model is applied to represent data in DW images for multiple b values (at least two b values) at the same position. Gaussian diffusion is the most widely used model. However, in practice, diffusion cannot be simply represented by Gaussian model because the microenvironment in biological tissues is too complex to be reflected and evaluated a mono-exponential decay, bi-exponential

decay and tri-exponential decay. Thus, non-Gaussian models supported by different physical insights were developed, such as the stretch model, fractional order calculus (FROC) model, continuous-time random-walk (CTRW) model, fractional motion (FM) model and kurtosis model.

In addition, IVIM introduced by D. Le Bihan in 1988, includes two components in decay curve that are respectively corresponding to perfusion and diffusion have different decay manners. The perfusion decays faster and diffusion decays slower. A bi-exponential model, therefore, has been built, as illustrated in

$$\frac{S}{S_0} = f \cdot e^{-bD_1} + (1-f) \cdot e^{-bD_2} \qquad (3\text{-}10)$$

where f is the volume fraction between diffusion and perfusion, D_1 and D_2 are diffusion constant respectively corresponding to diffusion and perfusion [19]. A set of bi-exponential decay curves are shown in Fig 3-3 (B). Furthermore, bi-exponential theory has been extended to applications with intracellular and extracellular components [20].

However, in some cases, the fraction f in bi-exponential model is too flexible to hit the true value [21]. Thus, more sophisticated models have been developed to reflect the complicated microenvironments by diffusion properties. The stretched exponential model denoted as Equation (3-11) has been introduced to account for heterogeneity caused by multiple components of water diffusion in brain,

$$\frac{S}{S_0} = e^{-(bD)^{\alpha}} \qquad (3\text{-}11)$$

where α is a measure of tissue complexity and D is diffusion constant [22]. A set of stretched exponential decay curves are shown in Fig 3-3 (C). The stretch model has been used in brain studies, prostate cancer, liver fibrosis and nasopharyngeal carcinoma [23, 24, 25, 22, 26].

Furthermore, the FROC model denoted as Equation (3-12) has extended the stretch model using fractional order calculus to solve the Bloch-Torrey equation regarding time and space,

$$\frac{S}{S_0} = e^{-(b^\beta D_f(\mu^2/\Delta))^{1-\beta}}$$

(3-12)

where β is fractional order derivative in space and μ is a spatial parameter [27, 28]. A set of FROC model curves are shown in Fig 3-3 (D). FROC model has been used in brain tumor and breast lesion [29, 30]. Moreover, its associated model known as CTRW model, as denoted in Equation (3-13), has been built to generalize the random walk (RW) model that derives the feature of Brownian motion in practice,

$$\frac{S}{S_0} = E_\alpha(-(bD)^{\beta/2})$$

(3-13)

where E is Mittag-Leffler function, α and β are spatial and temporal fractional orders [21, 31, 32]. If only Gaussian diffusion and sub-diffusion properties of white matter (WM) and gray matter (GM) are considered, Equation (3-13) can be further condensed as [21],

$$\frac{S}{S_0} = E_\alpha(-bD)$$

(3-14)

A set of CTRW model curves are shown in Fig 3-3 (E). CTRW model has been used in identifying differences between low-grade and high-grade brain tumors in children [33].

Additionally, more models are used to target to specific cases, such as tri-exponential model in the liver, as denoted in

$$\frac{S}{S_0} = f_1 \cdot e^{-bD_1} + f_2 \cdot e^{-bD_2} + f_3 \cdot e^{-bD_3}$$

(3-15)

where the summation of f_1, f_2 and f_3 is 1 [34]. A set of tri-exponential curves are shown in Fig 3-3 (F).
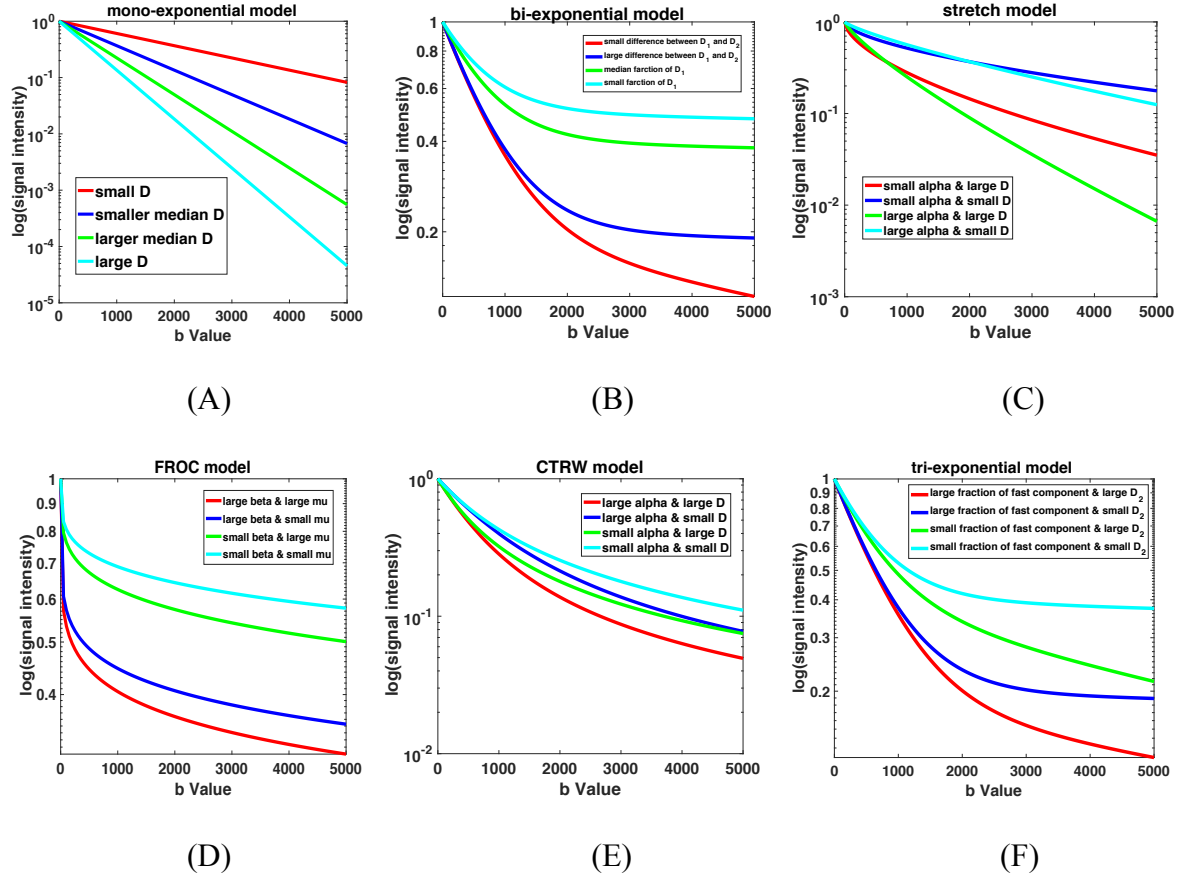
Figure 3 - 3 Simulation curves: (A) Simulation curves of mono-exponential model, (B) Simulation curves of bi-exponential model, (C) Simulation curves of stretch model, (D) Simulation curves of FROC model, (E) Simulation curves of CTRW model and (F) Simulation curves of tri-exponential model.

4. Diffusion MRI for characterizing white matter damage in ALS mouse model at High-b values

4.1 INTRODUCTION

White matter (WM) is composed of axons wrapped by myelin sheaths and located in brain and spinal cord [35]. Myelin, a complex fatty substance consisting of multiple lipid bilayers, is originated from myelin-generating cells that are Schwann cells in the peripheral nervous system and the oligodendroglial cells in the central nervous system [35, 36]. Damage of myelin sheaths is related to some neurodegenerative diseases, such as multiple sclerosis, multiple system atrophy and amyotrophic lateral sclerosis (ALS) [37, 38].

ALS is a fatal motor neuron disease and its etiology remains unknown [39]. It is characterized degeneration in upper and lower motor neurons located in primary motor cortex, brainstem and spinal cord [39, 40]. Clinically, ALS begins with muscle weakness that affects moving, talking and chewing or swallowing and then causes loss of mobility [41]. Ten percent (10%) of ALS cases are inheritable; that is known as familial ALS and ninety percent (90%) cases are not inheritable, as known as sporadic ALS. Many gene mutations contribute to develop this disease, such as superoxide dismutase 1 (SOD1), repeat expansions in gene encoding, TAR DNA-binding protein 43 and fused in sarcoma/translated in liposacoma [42]. The SOD1 mutations cause approximately 20% of familial ALS are one of the most frequently studied animal model in ALS, [43]. Specifically, SOD1 gene encodes a 153 amino acid metalloenzyme that catalyzes, with copper, the conversion of toxic superoxide radicals to hydrogen peroxide and oxygen [43, 44]. G93A-SOD1 that is replaced alanine by glycine at residue 93 is the mainly used mutant and shows hind limb weakness leading to paralysis and death [43, 44]. In addition, an

increasing number of variants of the original G93A-SOD1 animal models have been recently published (G93A, G37R, G85R and D90A) [43].

The diagnosis of ALS is based on the combination of clinical symptoms and examinations of upper motor neurons and lower motor neurons including electromyogram and nerve conduction studies, proton magnetic resonance spectroscopy (^{1}H-MRS), MRI and genetic testing [41]. In ^{1}H-MRS diagnosis, it has been demonstrated that N-acetylaspartate decreases and choline increases in both of basal ganglia and thalamus in ALS patients compared with controls [39]. In MRI, various techniques have been used, such as conventional MRI, functional MRI (fMRI), magnetization transfer (MT) imaging and diffusion tensor imaging (DTI) [40]. Although earlier studies have shown signal intensity changes along corticospinal tract (CST) by T_2-weighted, proton-density weighted MRI and T_2-weighted fluid-attenuated inversion recovery imaging, conventional MRI techniques suffer from low sensitivity in ALS detection [45, 46, 47, 48]. Moreover, Bahram Mohammadi and coworkers have demonstrated changes in premotor cortex as well as a reduction of activity in the default mode network in ALS patients by resting-state fMRI [49]. MT imaging studies that provide a better sensitivity and specificity have illustrated a significant reduction of MT ratio in CST from ALS patients [50, 51, 52]. On the other hand, DTI has become a popular MRI diagnosis approach, due to its relatively easy implementation in clinical settings. Some studies have been reported decreasing fractional anisotropy (FA) and increasing mean diffusivity (MD) along CST in ALS patients [53, 54, 55]. More remarkably, correlations between DTI parameters and the measure of the disease severity and duration has been built [53]. However, the correlation and MD has not demonstrated been reliable or consistent across other studies [56, 57].

The current DTI for ALS exploit directional restricted diffusion of water as a contrast. Nevertheless, there are few diffusion studies of myelin, the damaged site of white matter disease. Myelin is composed chiefly of large molecules, such as lipid and lipoproteins. As mentioned in section 3.2, diffusion behaviors of macromolecules vary with plenty of factors. Thus, myelin damage in ALS potentially reflect in altered diffusion properties. However, there are few studies on myelin diffusion properties in ALS. Additionally, low diffusivities of lipids make signal intensities of myelin high enough to be detected under ultra-high b condition. The hypothesis of this study is that high b-value diffusion MRI can be used to evaluate alterations of the spinal cord in a transgenic mouse model of ALS (G93A-SOD1).

4.2 MATERIALS AND METHODS

4.2.1 Sample Preparation

Based on genotyping protocols, two groups of animals were bred for this study: An ALS mutant group (G93A-SOD1) (n = 5) and a wild type control (WT) littermate mice group (n = 6) Mice in both groups were euthanized by CO_2 inhalation and transcardially perfused with phosphate buffered saline (PBS) and 4% paraformaldehyde (PFA) solution when they reached their symptomatic stage, at postnatal day 150 (P150).

4.2.2 MRI Scans

All MRI measurements were performed using a 9.4 T MRI scanner (Agilent, Santa Clara, CA) and, in each scan, two mice were carefully aligned and simultaneously scanned to get the two spinal cords in the same image.

A diffusion weighted STEAM sequence (Fig 4-1) was applied with following parameters:

Table 4. 1 Acquisition parameters of diffusion weighted STEAM sequence

TR (ms)	TE (ms)	Δ (ms)	Δ (ms)	Field of view (FOV) (mm)	Slice thickness (ms)	Matrix size	Average
2000	30.5	400	11	32 x 50	1.5	64 x 96	25

The resolution of the diffusion weighted images was $0.5 \times 0.52 \times 1.5 \; mm$. Thirty (30) b-values were applied ranging from 0 to 858,022 s/mm^2 with a maximal diffusion gradient strength of 50 Gauss/cm. Two diffusion gradient directions, parallel and perpendicular to the long axis of the spinal cord, were applied. The total scan time for diffusion weighted images was 23 hours 28 minutes each time.
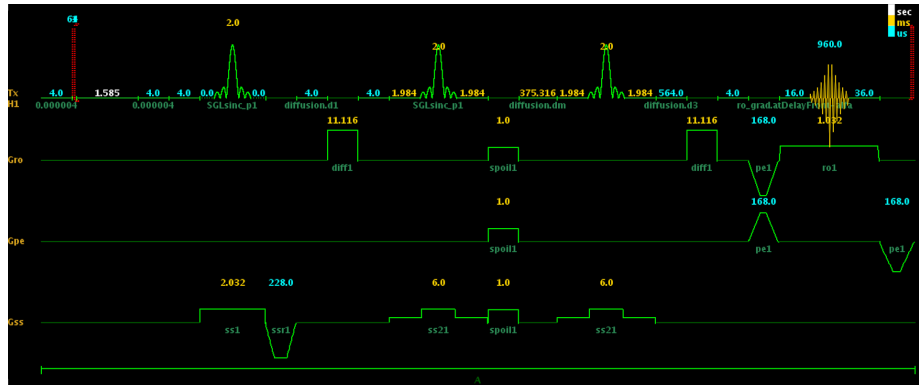
(A)
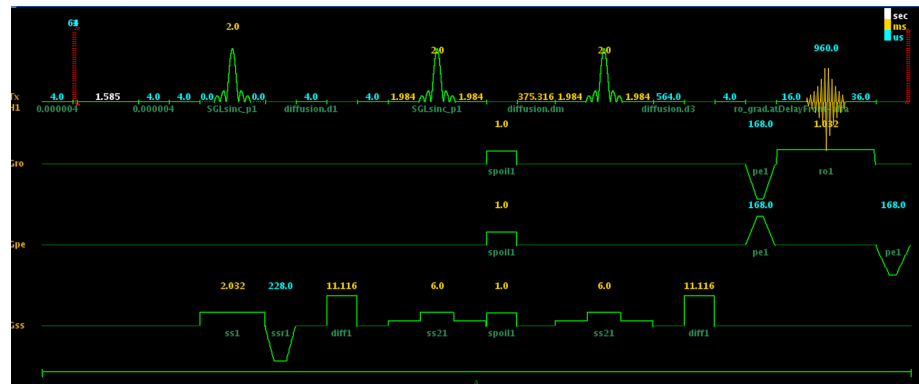
(B)

Figure 4 - 1 Diagram of the STEAM based diffusion-weighting pulse sequence in the direction (A)

parallel to the long axis of the spinal cord and (B) perpendicular to the long axis of the spinal

cord.

Fast spin echo sequences with parameters: TR/TE = 1000/12 ms, echo train length = 8,

matrix = 192 × 256, FOV = 36 × 50 mm, slice thickness = 1.5 mm, averages = 2, were employed

to acquire T_2 weighted images. The total scan time for T_2 weighted images was six minutes and

27 seconds each time.

4.2.3 Image Analysis

Image analysis was performed in Matlab (R2016a, MathWorks). The regions of interest

(ROIs) manually drawn at lumbar level from spinal cords of both diseased and control mice.

Signal-noise-ratios (SNRs) were calculated from the ROIs by

$$SNR = \frac{S_{mean}}{\sigma_{noise}} \qquad (4\text{-}1)$$

where S_{mean} was the mean image intensity in ROI and σ_{noise} was the standard deviation of the

ROIs drawn at four corners on the image. Two common diffusion models, bi-exponential

(Equation 4-2 (a)) and CTRW (Equation 4-2 (b)) model, were applied to the ROIs at lumbar

level and voxel-wisely in spinal cord,

$$\frac{S}{S_0} = f \cdot e^{-bD_{fast}} + (1-f) \cdot e^{-bD_{slow}} \qquad (4\text{-}2 \text{ (a)})$$

$$\frac{S}{S_0} = E_\alpha(-bD) \qquad (4\text{-}2 \text{ (b)})$$

where S and S_0 were the signal intensities with and without diffusion gradient applied, f was the

volume fraction between fast decay component and slow decay component, D_{fast} was the

diffusion fast decay component, D_{slow} was the diffusion constant of slow decay component, E

was Mittag-Leffler function, D was the diffusion constant and α was temporal fractional order. Moreover, a bi-component model combining CTRW and mono-exponential model was built and evaluated, as denoted in

$$\frac{S}{S_0} = f \cdot E_\alpha(-bD_{fast}) + (1-f) \cdot e^{-bD_{slow}} \qquad (4\text{-}3)$$

The least square curve fitting algorithm (lsqcurvefit) was used for nonlinear fitting. For bi-exponential model fitting, two methods were used. One was 1-step fitting which fitted all three parameters, f, D_{fast} and D_{slow}, into the least square curve fitting algorithm. The D_{fast} initial was evaluated by a mono-exponential model using the data points with b value from 0 to 34, 321 s/mm^2. The D_{slow} initial was evaluated by a mono-exponential model using the data points with b value from 308, 888 to 858,022 s/mm^2 and the f initial was evaluated by the intersection point of the mono-exponential and the y-axis. The other method was 2-step fitting. The first step evaluated the D_{slow} and f by a mono-exponential model using the data points with b value from 308, 888 to 858,022 s/mm^2. The second step took the evaluated D_{slow} and f as constants and only one parameter D_{fast} was fitted into the least square curve fitting algorithm. For CTRW model fitting, the D initial was evaluated by mono-exponential model using the data points with b value from 0 to 34, 321 s/mm^2. For the bi-component model, the D_{fast} initial was evaluated by a mono-exponential model using the data points with b value from 0 to 34, 321 s/mm^2. The D_{slow} initial and the f initial was evaluated by a mono-exponential model using the data points with b value from 308, 888 to 858,022 s/mm^2. Mean squared error (MSE) was used to evaluate models in the ROIs.

4.2.4 Histology

After completion of MRI scanning, spinal cords (SC) from each animal were dissected and removed using microsurgical techniques and placed in PFA for 48hs and then placed in PBS

1x. Two mice, one from the control group and one from the diseased group, were sent for basic myelin staining. SC were placed in progressive solutions of sucrose [5-30%] for an additional 24 hours for cryo-protection and sectioning. After embedding in optical cutting temperature (OCT) polymer compound (Tissue Tek, Sakura, Finetek, cat #4583) tissues were sectioned 50 μm thick using a microtome at -20 Celsius (Leica cryostat CM 1850 Cryostat, Buffalo Grove, IL). SC were sectioned longitudinally to anatomically match imaging data obtained during the MRI sessions. Sections were directly mounted on slides (Fisher brand Superfrost, cat# 12-550-15) and dried out for 15 minutes. Then, OCT residue was removed by washing three times for 10 min with Tris base buffer (TBS). Slides from WT and G93A-SOD1 groups were simultaneously immersed back-to-back in a 2% solution osmium tetroxide (OsO_4) for 30 minutes and then washed 3 times with PBS for 10 minutes. ROIs centered in lumbar SC regions were immediately acquired at 10x by light microscope attached to an optical camera and processed using ImageJ software (NIH freeware, Bethesda, MD).

4.2.5 Statistical Analysis

The student's t-test was applied to determine if the parameters extracted from each of the three diffusion models can differentiate diseased from control animals. The decision that two data sets are significantly different will be made when the common significant level p is smaller than 0.05. All the results were calculated using Microsoft Excel.

4.3 RESULTS

4.3.1 Diffusion Weighted Imaging

Representative images of diseased (arrow pointed) and control mice are shown in Fig 4-2. The ROIs at lumbar level for the two mice are shown in Fig 4-2 (A). In the T_2-weighted images (Fig 4-2 (B)), similar image intensities were observed in spinal cord at lumbar level of the

diseased and control animals but in the diffusion-weighted images (Fig 4-2 (C), (D), (E), (F)), the control animal showed relatively higher signals. Moreover, with the b value increased (Fig 4-2 (E), (F)), the differences of image intensities between two mice were larger.
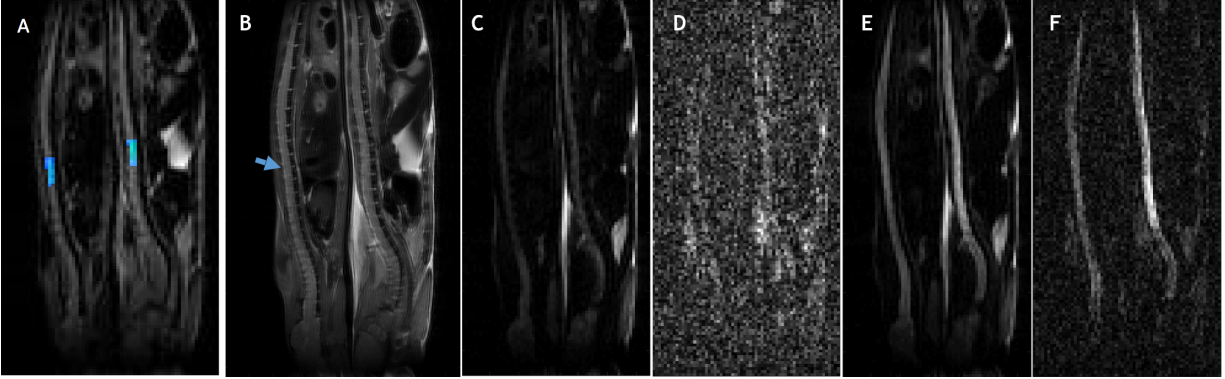
Figure 4 - 2 Sagittal MR images of the representative mice: (A) The ROIs at lumbar level (B)Anatomical image (T2 weighted) with the diseased mouse (arrow pointed) and control. (C) Diffusion weighted images at b = 1.34 × 10⁴ s/mm² with the diffusion-weighting direction parallel to the long axis of the spinal cord. (D) Diffusion weighted image at b = 8.58 × 10⁵ s/mm² with the diffusion-weighting direction parallel to the spinal cord. (E) Diffusion weighted image at b = 1.34 × 10⁴ s/mm² with the diffusion-weighting direction perpendicular to the spinal cord. (F) Diffusion weighted image at b = 8.58 × 10⁵ s/mm² with the diffusion-weighting direction perpendicular to the spinal cord.

In the diffusion-weighted images at the same b value (Fig 4-2 (C), (E) and (D), (F)), the spinal cords in the images with a diffusion-weighting direction perpendicular to the spinal cord have higher signal intensities. With the SNRs greater than 10, mean signal intensities in the ROIs at the lumbar level of spinal cord were found lower for the diseased mouse than for the control mouse at all the b values (Fig 4-3). In addition, the mean signal intensities were much higher in

both animals with the diffusion gradients applied perpendicular to long axis of the spinal cord than with parallel diffusion-weighting direction (Fig 4-3).
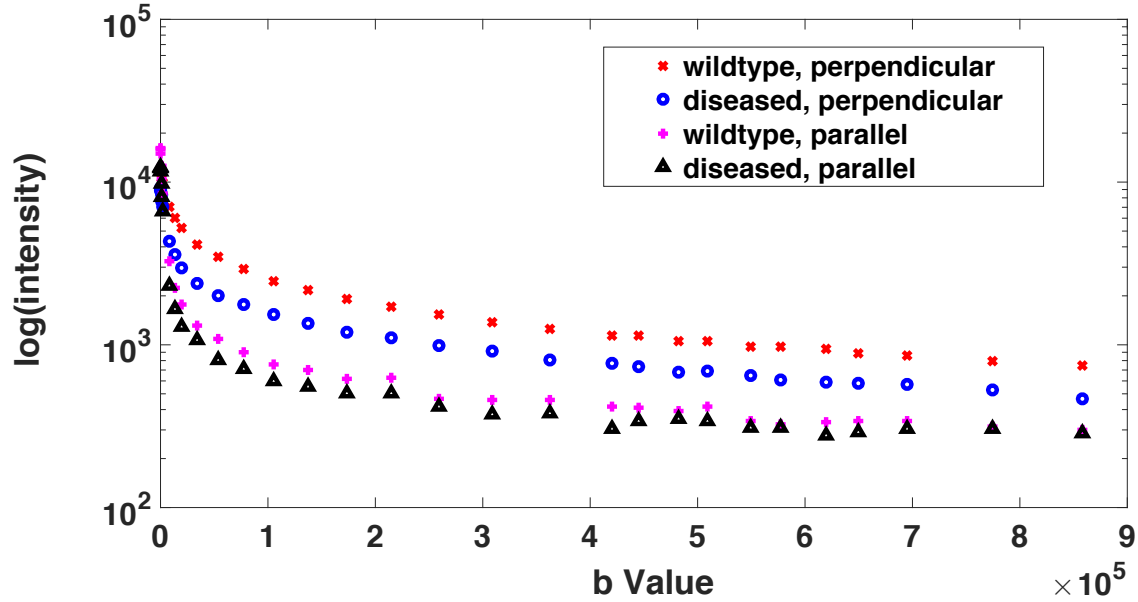
Figure 4 - 3 Log-scaled signal decay plot as a function of b-value for selected ROIs at lumbar level of the spinal cords of representative diseased and control mice with perpendicular and parallel diffusion gradients respectively.

4.3.2 Model Fitting

Representative parameter maps extracted from bi-exponential model were shown in Fig 4-4 (B), (C), (D) and Fig 4-5 (B), (C), (D). The diseased animal on the left had relatively low fractions (Fig 4-4 (B) and Fig 4-5 (B)) and high diffusion constant values of the fast decay component (Fig 4-4 (C) and Fig 4-5 (C)) in spinal cord at lumbar level. The diffusion constant values of the slow decay component (Fig 4-4 (D) and Fig 4-5 (D)) were similar for the diseased and control animals.

Figure 4 - 4 The parameter maps for representative diseased (arrow) and control mice in spinal cord with the perpendicular diffusion gradient using bi-exponential model by 1-step fit: (A) anatomical image, (B) fraction of the fast decay component map, (C) diffusion constant map of fast decay component, and (D) diffusion constant map of slow decay component.

Figure 4 - 5 The parameter maps for representative diseased (arrow) and control mice in spinal cord with the perpendicular diffusion gradient using bi-exponential model by 2-step fit: (A) anatomical image, (B) fraction of the fast decay component map, (C) diffusion constant map of fast decay component, and (D) diffusion constant map of slow decay component.

Representative parameter maps of CTRW model were shown in Fig 4-6 (B) and (C). The diseased animal on the left had relatively high diffusion constant values (Fig 4-6 (C)) in spinal cord at lumbar level. The α values (Fig 4-6 (B)) were similar for the diseased and control animals.
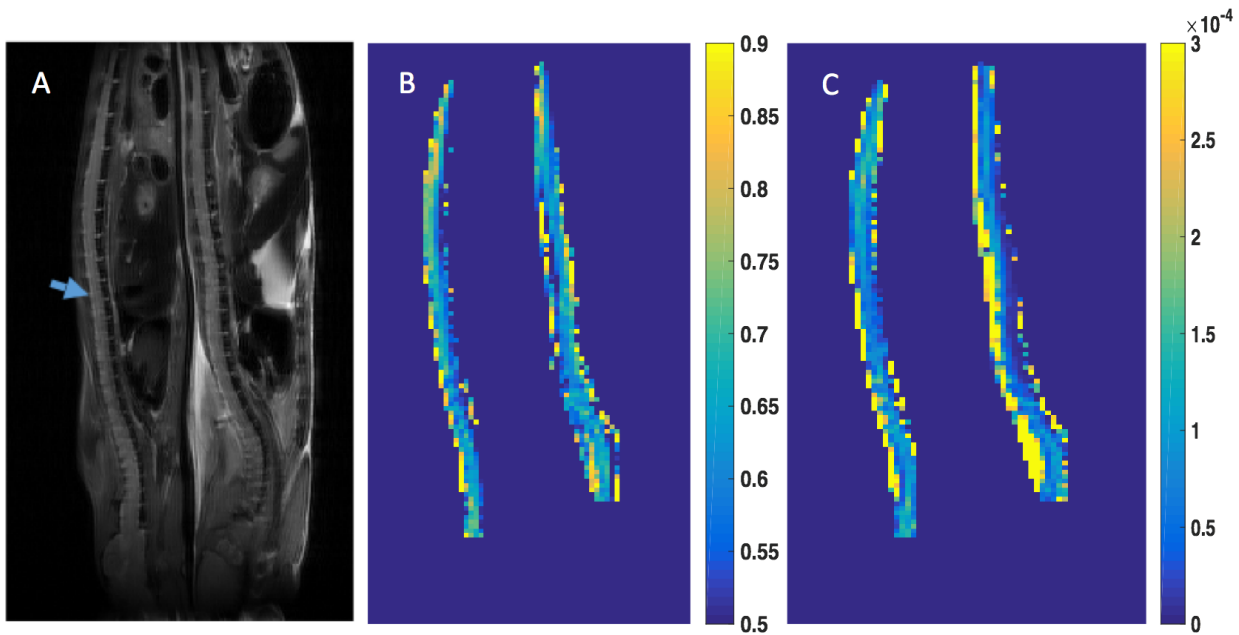
Figure 4 - 6 The parameter maps for representative diseased (arrow) and control mice in spinal cord with the perpendicular diffusion gradient using CTRW model: (A) anatomical image, (B) α map, and (C) diffusion constant map.

The representative parameter maps of bi-component model were shown in Fig 4-7. The diseased animal on the left had relatively low fractions (Fig 4-7 (C)) and high diffusion constant values of the fast decay component (Fig 4-7 (B)) at lumbar level. The α values (Fig 4-7 (A)) and diffusion constant values of the slow decay component (Fig 4-7 (D)) were similar for the diseased and control animals.
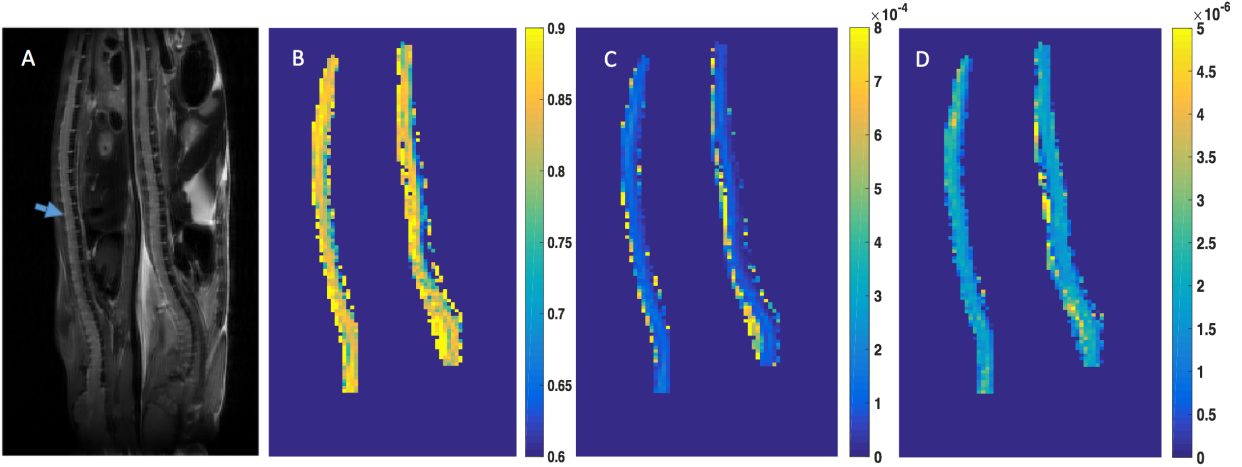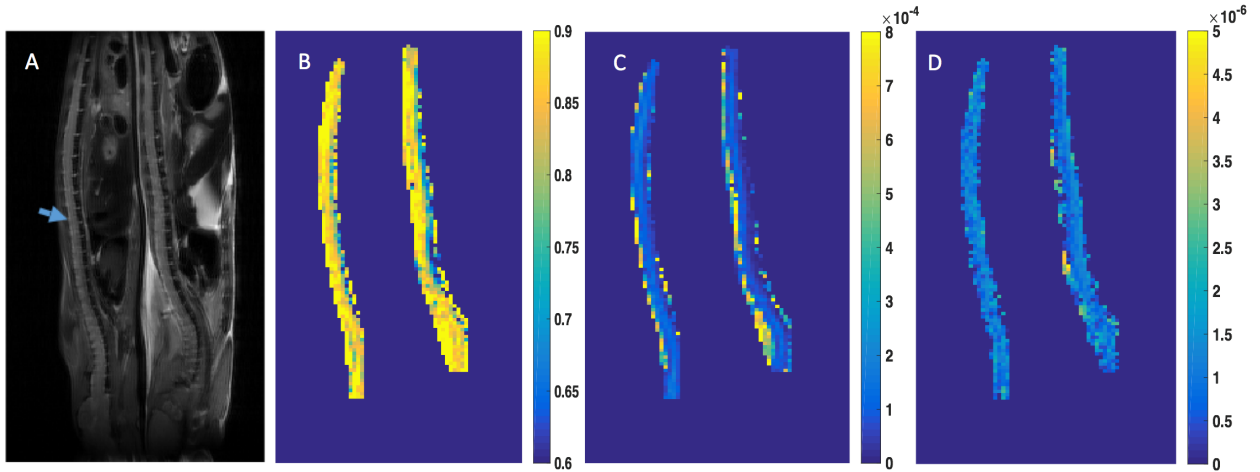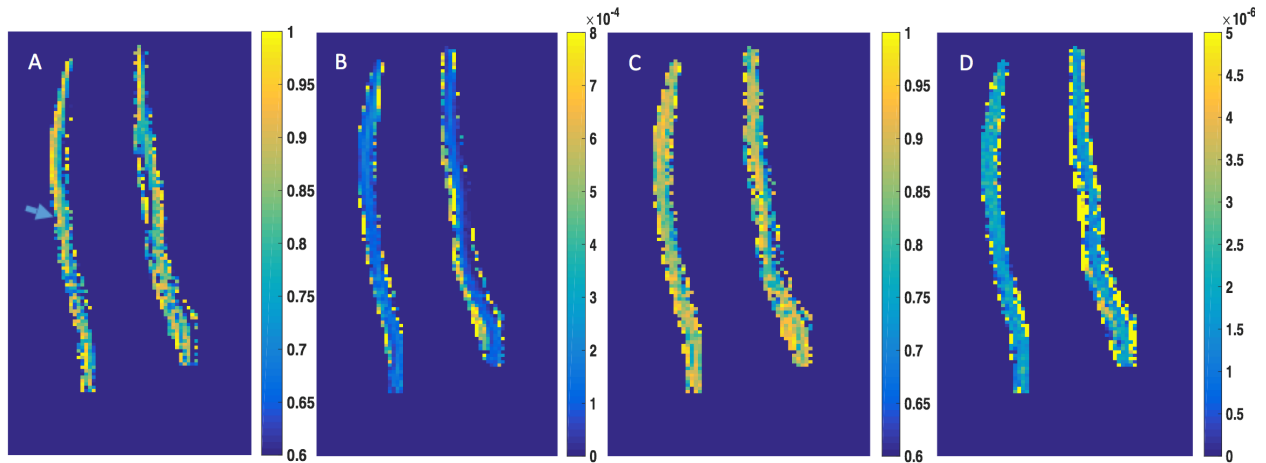
Figure 4 - 7 The parameter maps for representative diseased (arrow) and control mice in spinal cord with the perpendicular diffusion gradient using bi-component model: (A) α map, (B) diffusion constant map of fast decay component, (C) fraction of the fast decay component map, and (D) diffusion constant map of slow decay component.

The error maps of the three models for representative diseased and control mice in spinal are shown in Fig 4-8. The error map of bi-exponential model by 2-step fit had relative large values (Fig 4-8 (B)) and the error map of bi-exponential model by 1-step fit had smaller values than by 2-step fit (Fig 4-8 (A)). The error map of CTRW model (Fig 4-8 (C)) had similar values with the error map of bi-exponential model by 1-step (Fig 4-8 (A)). The error map of bi-component model had the smallest values than the other two models.

Figure 4 - 8 The error maps of (A) bi-exponential model by 1-step fit, (B) bi-exponential model by 2-step fit, (C) CTRW model, and (D) bi-component model for representative diseased and control mice in spinal cord with the perpendicular diffusion gradient.

In the ROIs at lumbar level, the bi-component model (Fig 4-9 (D)) showed a better fit than bi-exponential model (Figure 4-9 (A), (B)) and CTRW model (Fig 4-9 (C)) at increasing b-values for data with the diffusion-weighting direction perpendicular to the spinal cord.

(A)
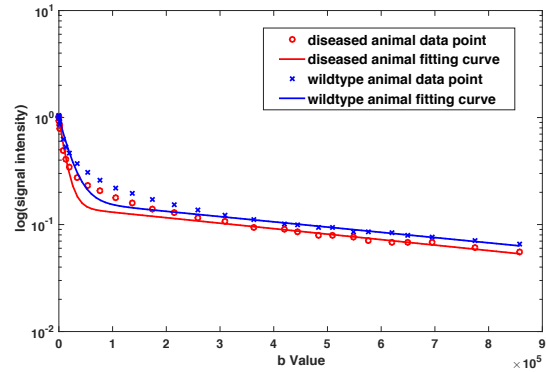
(B)
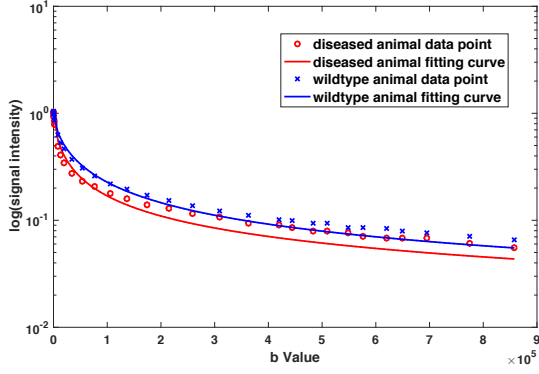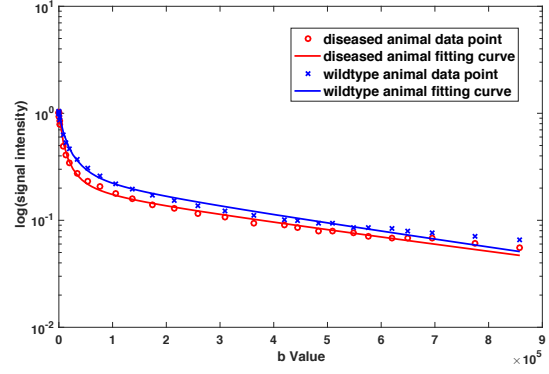
(C)   (D)

Figure 4 - 9 Plot of representative diseased and control mice in ROIs at lumbar level with the
perpendicular diffusion gradient using (A) bi-exponential model by 1-step fit, (B) bi-exponential
model by 2-step fit, (C) CTRW model, and (D) bi-component model.

4.3.3 Comparison between Models

Compared to bi-exponential model (Fig 4-10 (A), (B)) and CTRW model (Fig 4-10 (C)),
bi-component model (Fig 4-10 (D)) had much smaller mean squared errors (MSEs) in both
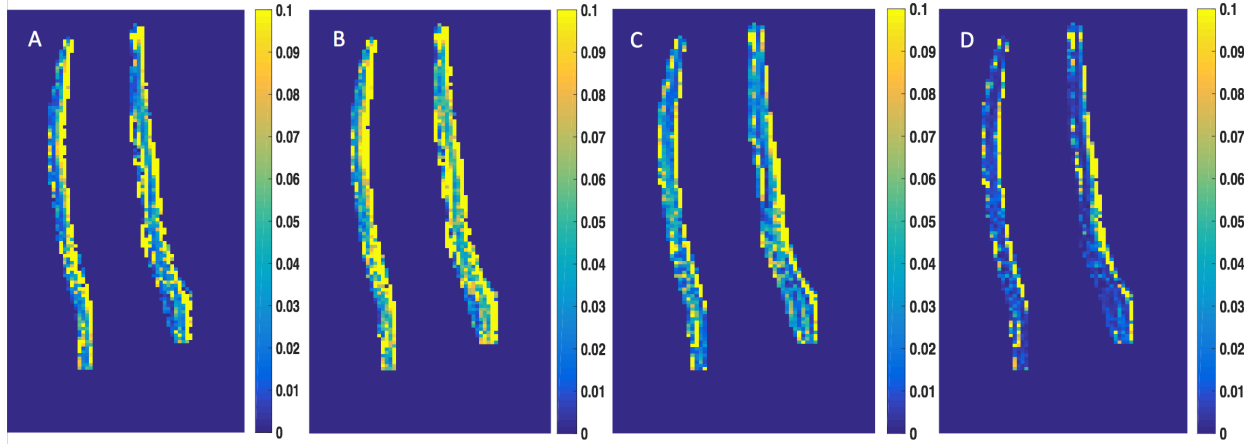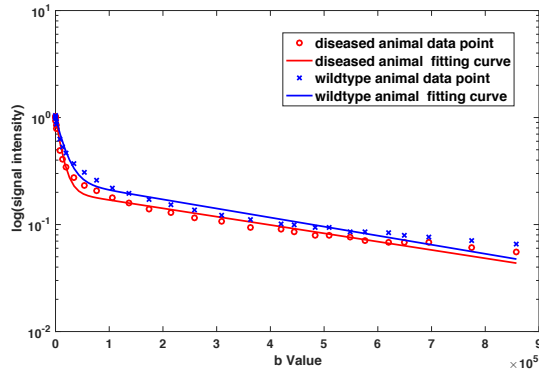control and diseased animals.
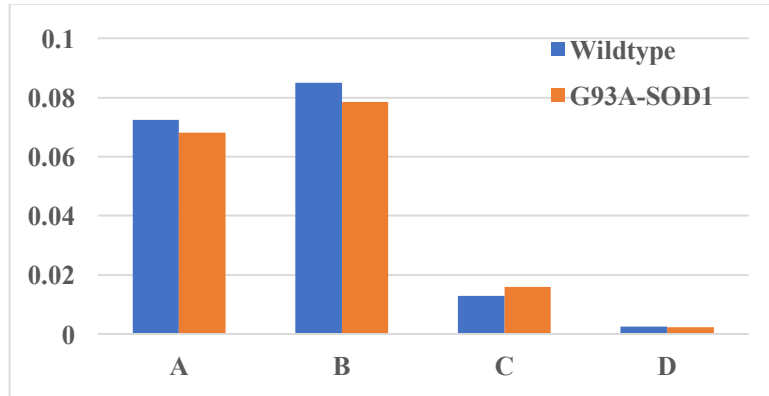
Figure 4 - 10 Fitting MSEs of (A) bi-exponential model by 1-step fit, (B) bi-exponential model by
2-step fit, (C) CTRW model, and (D) bi-component model in spinal cord at lumbar level of
diseased and control animals with the perpendicular diffusion gradient.

36

4.3.4 Comparison between Control and Diseased Animals

The parameters of bi-exponential model showed no significant differences between diseased animals and control animals (as shown in Fig. 11).

(A)

(B)

(C)

(D)

(E)

(F)
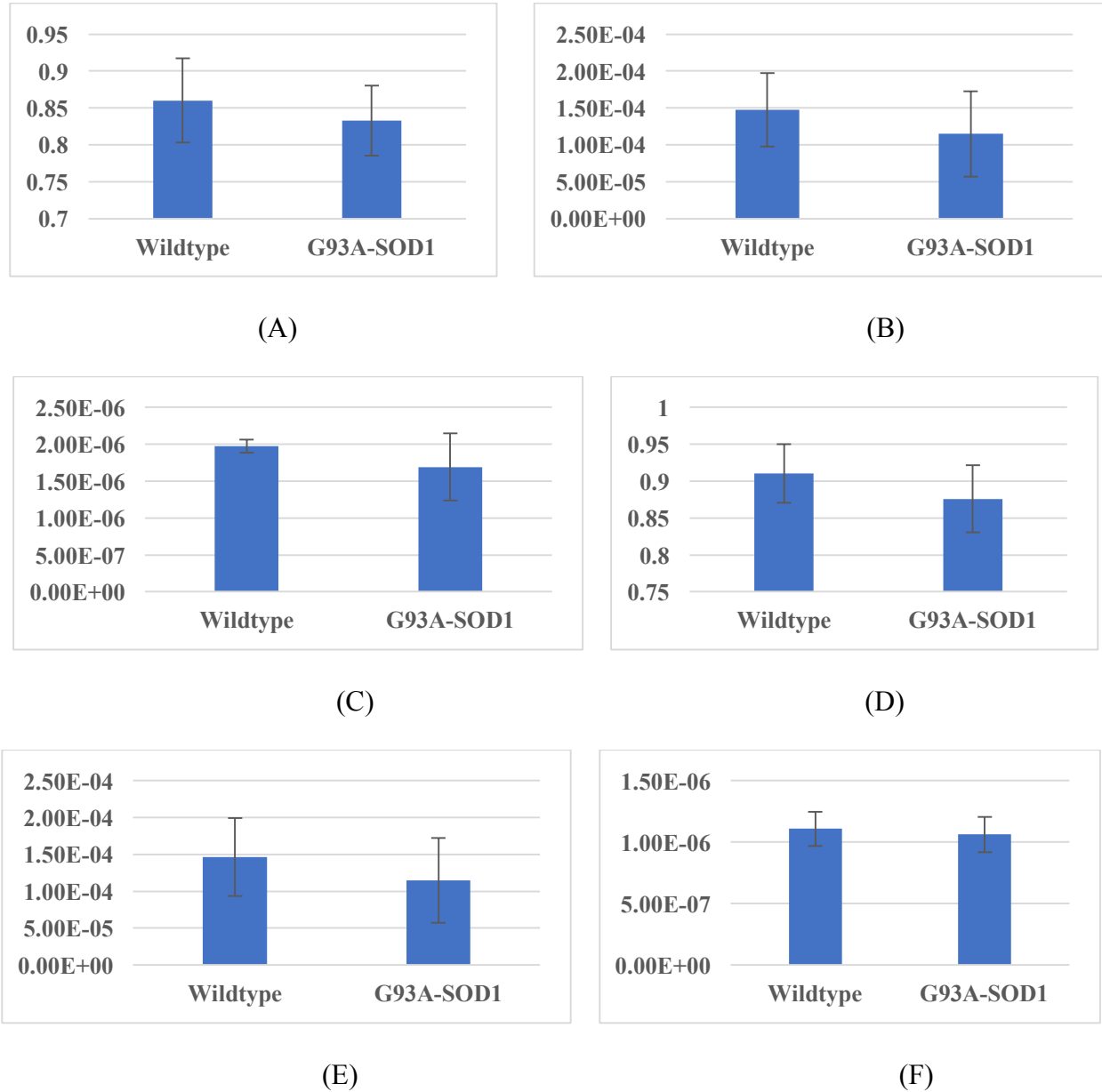
Figure 4 - 11 The comparison of diseased (n = 5) and control (n = 6) mice for fitting results extracted from bi-exponential model: (A) fractions of fast decay component with p=0.38 in t-test in bi-exponential model by 1-step fit, (B) diffusion constant values of fast decay component with

$p = 0.32$ *in t-test in bi-exponential model by 1-step fit, (C) diffusion constant values of slow decay component with* $p = 0.21$ *in t-test in bi-exponential model by 1-step fit, and (D) fractions of fast decay component with* $p = 0.20$ *in t-test in bi-exponential model by 2-step fit, (E) diffusion constant values of fast decay component with* $p = 0.35$ *in t-test in bi-exponential model by 2-step fit, (F) diffusion constant values of slow decay component with* $p = 0.59$ *in t-test in bi-exponential model by 2-step fit.*

The parameters of CTRW model (Fig 4-12) showed no significant differences between diseased animals and control animals.

(A)   (B)
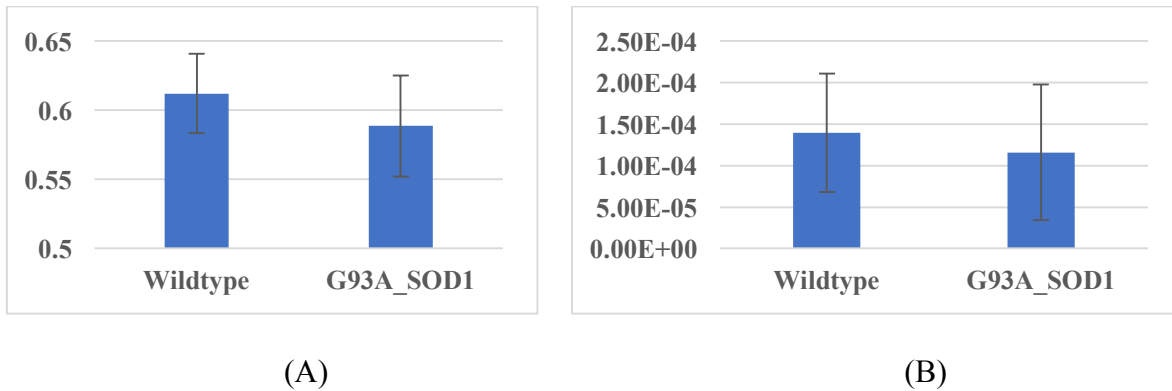
Figure 4 - 12 The comparison of diseased (n = 5) and control (n = 6) mice for fitting results extracted from CTRW model: (A) α values with p=0.24 in t-test, and (B) diffusion constant values with p=0.61 in t-test.

The parameters of bi-component model (Fig 4-13) showed no significant differences between diseased animals and control animals.

(A)

(B)

(C)

(D)
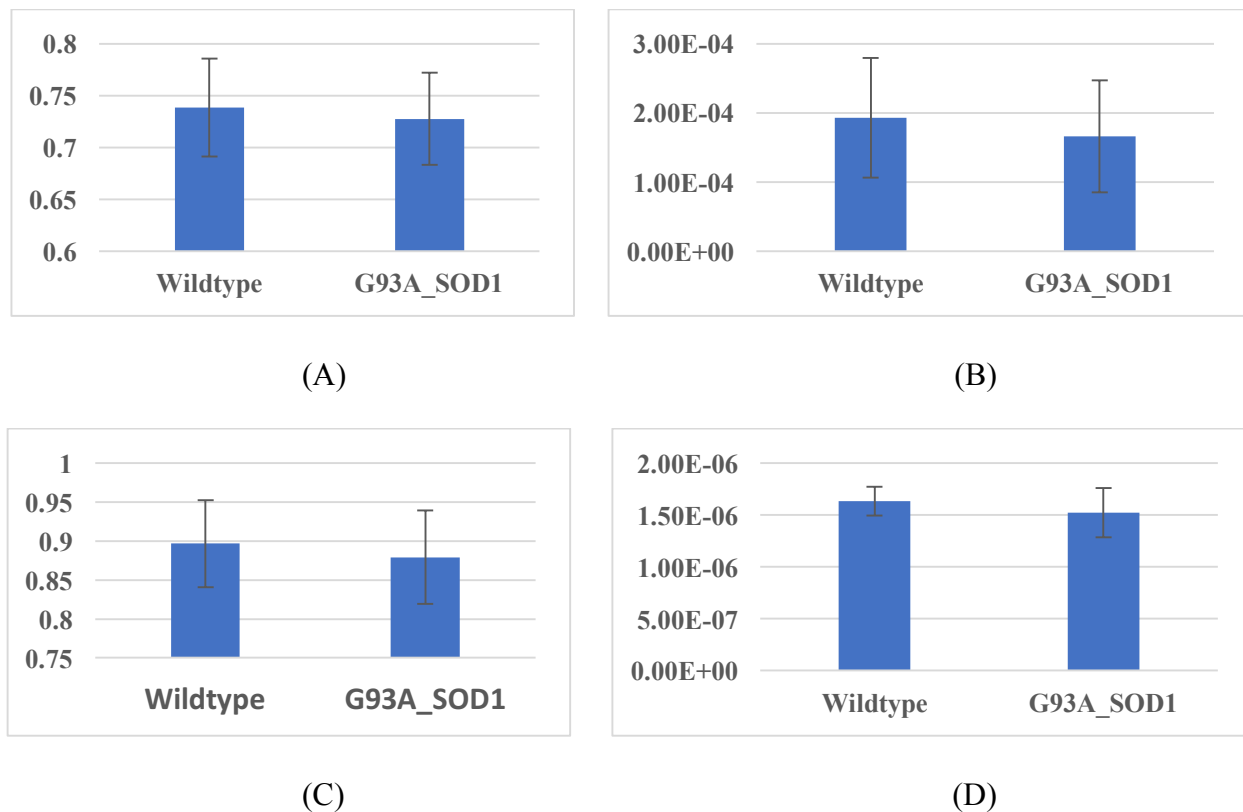
Figure 4 - 13 The comparison of diseased (n = 5) and control (n = 6) mice for fitting results extracted from bi-component model: (A) α values with p=0.69 in t-test (B) diffusion constant values of fast decay component with p=0.59 in t-test, (C) fractions of fast decay component with $p = 0.61$ in t-test, and (D) diffusion constant values of slow decay component with $p = 0.36$ in t-test.

4.3.5 Histology

Axonal fiber morphology and integrity of the spinal cords were validated by histological analysis (Figure 4-14). Sagittal section of the spinal cord in a wild type mouse (Figure 4-9 (A)) showed an intensive Myelin staining (Osmium tetroxide) in grey and white matter areas at lumbar segment. A significant decrease was observed in WM myelin staining in G93A-SOD1 mice located in comparable WM areas at the same level segment.
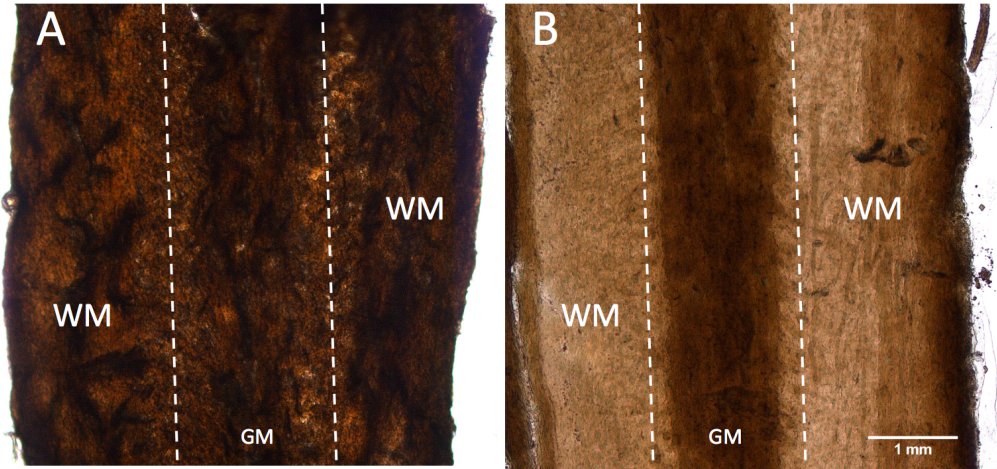
Figure 4 - 14 Histological analysis of (A) control (wild type) and (B) diseased (G93A-SOD1) mice.

4.4 DISCUSSION

At high b values (up to 8.58×10^5 s/mm^2) achieved by STEAM based diffusion-weighting pulse sequence, we found differences of signal intensities at lumbar level between diseased and control animals (Fig 4-2 (E), (F)). With b-value increasing, signals from most of water gradually decayed away and signals from fat tissues remained due to the slow diffusivities (Fig 4-2 (E)). With the further increasing of b-value, the subcutaneous fat tissues started decaying away (Fig 4-2 (F)). However, the myelin in spinal cord decayed much slower than the subcutaneous fat because of the highly-restricted structure in spinal cord. Since myelin contributed the most of signal intensities at high b values, these differences could reflect the myelin damages in spinal cord caused by ALS.

Furthermore, we observed differences of signal intensities in diffusion weighted images of spinal cord in same animal at same high b values (e.g., $b = 1.34 \times 10^4$ s/mm^2) but with two different directions (parallel or perpendicular to long axis of the spinal cord), which might indicate diffusion of myelin in spinal cord is largely direction dependent, as shown in Fig 4-2 (C),

(E) and (D), (F). As reported in literature, the lipid molecules on membrane have two types of diffusion, lateral diffusion and transverse diffusion ('flip-flop') [58, 59]. The lateral diffusion refers to lipid molecules diffusing in the plane of membrane, while the transverse diffusion is lipid molecules moving from one surface of the membrane to the other side [58, 59, 60]. The transverse diffusion was reported much slower than the lateral diffusion [60, 61, 62]. Moreover, thin layers of water exist between myelin sheaths [63]. The diffusion of the thin layers of water that can be highly directionally restricted, might contribute to the detected signals as well [63]. Since the gradient paralleled to long axis of spinal cord probes lateral diffusion and the gradient perpendicular to long axis of spinal cord detects transverse diffusion, the direction dependence of diffusion signal decay can indicate the bilayer structure of myelin. In addition, the changes on the directional dependence of diffusion has potential to reflect the changes of myelin structure with the progression of the white matter damage.

With a further observation of measured signal intensities from an ROI drawn at the lumbar level of the spinal cord (Fig 4-3), we found that the data didn't follow the mono-exponential decay with b-value increasing. Instead, the curves indicated two components, curving behaviors in front part and a flat tail. Thus, we used the bi-exponential model (Equation 4-2 (a)) to fit the data. The slow decay component could be related to the myelin signal decay in spinal cord. The fast decay component could be corresponding to water signal and subcutaneous fat decay. At first, the bi-exponential model with three parameters fitting which was denoted as bi-exponential model by 1 step fit in section 4.3 was used. Nevertheless, due to the nature of nonlinear fitting algorithm, the tail where data points had small values was given a small weight because of smaller squared errors. Thus, 2 steps bi-exponential model fitting was used to improve the bad fit on tail. As a result, squared errors increased but the tail had an equal weight

and fitting parameters were reduced from three to two. However, more importantly, the first mono-exponential decay in bi-exponential model cannot represent the fast decay component very well due to the curving area ($b < 308, 888$ s/mm^2). Therefore, CTRW model (Equation 4-2 (b)), a sophisticated model considered heterogeneity caused by multiple components, was used. It gave a better fit on the curving area and also had much smaller MSEs than bi-exponential model. Nevertheless, it decayed too fast at high b values, which means the CTRW model cannot represent the entire data set. At last, we built a bi-component model (Equation 4-3) combined with CTRW and mono-exponential models. The water and fat signal contributions could be represented by CTRW model. The myelin signals at high b values could be described by mono-exponential model. Consequently, the MSEs of this bi-component model fitting decreased dramatically and it had a better fit on both the curving area and tail than bi-exponential and CTRW model.

Unfortunately, no significant difference between diseased from control animals was found in all three models. As mentioned above, the bi-exponential and CTRW models cannot represent data well. In the bi-component model, the CTRW decay in the first part has already considered partial contributions of myelin. So, it might be a double-counting problem for adding a mono-exponential decay in the second part that was designed to account for the entire contributions of myelin. Additionally, the small sample size and small diameter in spinal cord might be other factors interfering with the measurements.

4.5 CONCLUSION

In summary, this study demonstrated the feasibility of high b-value diffusion MRI to evaluate spinal cord alterations in a symptomatic mouse model of ALS. We found the differences of signal intensities in spinal cord at lumbar level between control and diseased mice

in diffusion weighted images at high b values, which could reflect the myelin damage of ALS. We further found differences of the signal intensities in diffusion weighted images with the gradient parallel and perpendicular to the long axis of spinal cord, which might indicate myelin diffusion in spinal cord is direction dependent. In addition, a new bi-component model was introduced to provide a good fit of the data with small MSEs and a new perspective to explain the data.

5. CONCLUSION

5.1 SUMMARY

In this study, we investigated spinal cord diffusion behaviors in wildtype and G93A SOD1 mouse model of ALS at multiple ultra high b values. Compared with the low b values (<6000 s/mm^2), high b values enable most of water signal decaying away while the signal for lipid persisted. Moreover, ultra high b values are high enough to ensure that most of the lipid signals decay but not the signals from myelin due to highly restricted structure in spinal cord. Thus, compared with DTI studies with water diffusion as contrast, this study focuses on the myelin that directly relates to this disease. Combining ultrahigh b values diffusion with a strong magnetic field (9.4 T), the SNR is high enough to employ diffusion MRI to study spinal cord. Furthermore, we quantified the differences between diseased animals and controls at lumbar level by diffusion models. We also proposed a new diffusion model to represent and explain the data acquired in the experiments. Although the fitting results of this new model showed no significant difference between diseased animals from controls, it provided a better fit (small error) and a new perspective to explain the data (bi-component). Additionally, since the contrast in this work is the myelin sheaths, other spinal cord diseases related to myelin damages also can be studied by this high b-value diffusion MRI technique.

5.2 FUTURE WORK

This work is a pioneer study to evaluate spinal cord alterations due to myelin damages using ultrahigh b-value diffusion MRI. Therefore, new diffusion models that have more precise fit and enhanced physical insights are needed to differentiate and quantify the progression of ALS. Moreover, further studies of other diseases associated with white matter damage are needed to validate this approach of characterizing white matter damage.

6. REFERENCES

[1]   I. Niebroj-Dobosz, et al., "Myelin composition of spinal cord in a model of amyotrophic lateral sclerosis (ALS) in SOD1G93A transgenic rats," *Folia Neuropathologica,* vol. 45, pp. 236-241, 2007.

[2]   N. B. Smith, Introduction to Medical Imaging: Physics, Engineering and Clinical Applications, New York: Cambridge University Press, 2011.

[3]   R. R. Edelman, "The History of MR Imaging as Seen through the Pages of Radiology," *Radiology,* vol. 273, pp. 181-200, 2014.

[4]   Z.-p. Liang, "Principles of Magnetic Resonance Imaging," The Institute of Electrical and Electronics Engineers,Inc., 2000.

[5]   R. H. Hashemi, "MRI The Basics," Lippincott Williams & Wilkins, a Wolters Kluwer business, 2010.

[6]   E. M. Haacke, et al., Magnetic Resonance Imaging Physical Principles and Sequence Design, John Wiley & Sons, Inc., 1999.

[7]   P. C. Lauterbur, "Image Formation by Induced Local Interactions: Examples Employing Nuclear Magnetic Resonance," *Nature,* vol. 242, pp. 190-191, 1973.

[8]   M. A. Bernstein, et al., Handbook of MRI Pulse Sequences, Elsevier Academic Press, 2004.

[9]   M. F. Reiser, et al., Magnetic Resonance Tomography, Springer-Verlag Berlin Heidelberg, 2008.

[10] S. Mori, Introduction to Diffusion Tensor Imaging, Elsevier, 2009.

[11] J. Helenius, et al., "Diffusion-Weighted MR Imaging in Normal Human Brains in Various Age Groups," *AJNR Am J Neuroradiol,* vol. 23, pp. 194-199, 2002.

[12] R. S. Gawande, et al., "Role of diffusion-weighted imaging in differentiating benign and malignant pediatric abdominal tumors," *Pediatr Radiol,* vol. 43, pp. 836-845, 2013.

[13] A. Lehnert, et al., "Diffusion characteristics of large molecules assessed by proton MRS on a whole-body MR system," *Magnetic Resonance Imaging,* vol. 22, pp. 39-46, 2004.

[14] Z. Q. Ababneh, et al., "In vivo lipid diffusion coefficient measurements in rat bone marrow," *Magn Reson Imaging,* vol. 27, pp. 859-864, 2009.

[15] P. Cao, et al., "Diffusion magnetic resonance monitors intramyocellular lipid droplet size in vivo," *Magnetic Resonance Imaging,* vol. 73, pp. 59-69, 2015.

[16] D. C. Alexander and T. B. Dyrby, "Diffusion Imaging with Stimulated Echoes: Signal Models and Experiment Design," *arXiv preprint arXiv:1305.7367 [physics.med-ph],* 2013.

[17] N. A. Rangwala, et al., "Diffusion restriction in the human spinal cord characterized in vivo with high b-value STEAM diffusion imaging," *NeuroImage,* vol. 82, p. 416–425, 2013.

[18] D. Burstein, "Stimulated Echoes: Description. Applications. Practical Hints," *Concepts Magn. Reson.,* vol. 8, pp. 269-278, 1996.

[19] D. L. Bihan, et al., "Separation of Diffusion and Perfusion in Intravoxel Incoherent Motion MR Imaging," *Radiology,* vol. 168, pp. 497-505, 1988.

[20] T. Niendorf, et al., "Biexponential Difision Attenuation in Various States of Brain Tissue: Implications for Diffusion-Weighted Imaging," *Magn Reson Med,* vol. 36, pp. 847-857, 1996.

[21] C. Ingo, et al., "Parsimonious continuous time random walk models and kurtosis for diffusion in magnetic resonance of biological tissue," *Front Phys,* vol. 3, 2015.

[22] K. M. Bennett, et al., "Characterization of continuously distributed cortical water diffusion

rates with a stretched-exponential model," *Magn Reson Med,* vol. 50, pp. 727-734, 2003.

[23] X. Liu, et al., "Comparison of stretched-Exponential and monoexponential model diffusion-Weighted imaging in prostate cancer and normal tissues," *J Magn Reson Imaging,* vol. 25, pp. 1708-1713, 2015.

[24] S. W. Anderson, et al., "Characterizing non-gaussian, high b-value diffusion in liver fibrosis: Stretched exponential and diffusional kurtosis modeling," *J Magn Reson Imaging,* vol. 39, pp. 827-834, 2014.

[25] V. Lai, et al., "Intravoxel water diffusion heterogeneity MR imaging of nasopharyngeal carcinoma using stretched exponential diffusion model," *Euro Radiol,* vol. 25, pp. 1708-1713, 2015.

[26] M. G. Hall and T. R. Barrick, "From diffusion-weighted MRI to anomalous diffusion Imaging," *Magn Reson Med,* vol. 59, pp. 447-455, 2008.

[27] R. L. Magin, et al., "Anomalous diffusion expressed through fractional order differential operators in the Bloch–Torrey equation," *Journal of Magnetic Resonance,* vol. 190, pp. 255-270, 2008.

[28] X. Z. Zhou, et al., "Studies of Anomalous Diffusion in the Human Brain Using Fractional Order Calculus," *Magn Reson Med,* vol. 63, pp. 562-569, 2010.

[29] S. Yi, et al., "Differentiation of Low- and High- Grade Pediatric Brain Tumors with High b-Value Diffusionweighted MR Imaging and a Fractional Order Calculus Model," *Radiology,* vol. 277, pp. 489-496, 2015.

[30] S. Bickelhaupt, et al., "On a fractional order calculus model in diffusion weighted breast imaging to differentiate between malignant and benign breast lesions detected on X-ray

screening mammography," *PLoS One,* vol. 12, p. e0176077, 2017.

[31] C. Ingo, et al., "New Insights into the Fractional Order Diffusion Equation Using Entropy and Kurtosis," *Entropy,* vol. 16, pp. 5838-5852, 2014.

[32] M. M. Karaman, et al., "A fractional motion diffusion model for grading pediatric brain tumors," *MeuroImage: Clinical,* vol. 12, pp. 707-714, 2016.

[33] M. M. Karaman, et al., "Differentiating low- and high-grade pediatric brain tumors using a continuous-time random-walk diffusion model at high b-values," *Magn Reson Med,* vol. 76, pp. 1149-1157, 2016.

[34] J.-P. Cercueil, et al., "Intravoxel incoherent motion diffusion-weighted imaging in the liver: comparison of mono-, bi- and tri-exponential modelling at 3.0-T," *Eur Radiol,* vol. 25, pp. 1541-1550, 2015.

[35] C. M. Filley, Behavioral Neurology of White Matter, Oxford University Press, 2001.

[36] G. J. Siegel, et al., Basic Neurochemistry: molecular, cellular, and medical aspects, Lippincott Williams & Wilkins, 1999.

[37] B. Ettle, et al., "Oligodendroglia and Myelin in Neurodegenerative Diseases: More Than Just Bystanders?," *Mol Neurobiol,* vol. 53, pp. 3046-3062, 2016.

[38] S. G. Waxman, "Axonal conduction and injury in multiple sclerosis: the role of sodium channels," *Nat Rev Neurosci,* vol. 7, pp. 932-941, 2006.

[39] B. R. Foerster, et al., "25 years of neuroimaging in amyotrophic lateral sclerosis," *Nat Rev Neurol,* vol. 9, pp. 513-524, 2013.

[40] F. Agosta, et al., "The Present and the Future of Neuroimaging in Amyotrophic Lateral Sclerosis," *AJNR Am J Neuroradiol,* vol. 31, pp. 1769-1777, 2010.

[41] Gordon, PH, et al. "Amyotrophic Lateral Sclerosis Pathophysiology, Diagnosis and Management," *CNS Drugs,* vol. 25, pp. 1-15, 2011.

[42] T. Philips and J. D. Rothstein, "Rodent Models of Amyotrophic Lateral Sclerosis," *Curr Protoc Pharmacol,* vol. 69, pp. 1-21, 2015.

[43] L. V. D. Bosch, "Genetic Rodent Models of Amyotrophic Lateral Sclerosis," *Journal of Biomedicine and Biotechnology,* vol. 2011, p. 348765, 2011.

[44] R. A. Saccon, et al., "Is SOD1 loss of function involved in amyotrophic lateral sclerosis?," *Brain,* vol. 136, pp. 2342-2358, 2013.

[45] D. S. Goodin, et al., "Magnetic resonance imaging in amyotrophic lateral sclerosis," *Ann Neurol,* vol. 23, pp. 418-420, 1988.

[46] M. Hecht, et al., "MRI-FLAIR images of the head show corticospinal tract alterations in ALS patients more frequently than T2-, T1- and proton-density-weighted images," *J Neurol Sci,* vol. 186, pp. 37-44, 2001.

[47] M. Hecht, et al., "Hyperintense and hypointense MRI signals of the precentral gyrus and corticospinal tract in ALS: a follow-up examination including FLAIR images," *J Neurol Sci,* vol. 199, pp. 59-65, 2002.

[48] L. Zhang, et al., "The diagnostic utility of FLAIR imaging in clinically verified amyotrophic lateral sclerosis," *J Magn Reson Imaging,* vol. 17, pp. 521-527, 2003.

[49] B. Mohammadi, et al., "Changes of resting state brain networks in amyotrophic lateral sclerosis," *Exp Neurol,* vol. 217, pp. 147-153, 2009.

[50] Y. Kato, et al., "Detection of pyramidal tract lesions in amyotrophic lateral sclerosis with magnetization-transfer measurements," *AJNR Am J Neuroradiol,* vol. 18, pp. 1541-1547,

1997.

[51] J. L. Tanabe, et al., "Reduced MTR in the corticospinal tract and normal T2 in amyotrophic lateral sclerosis," *Magn Reson Imaging,* vol. 16, pp. 1163-1169, 1998.

[52] A. J. d. Rocha, et al., "Detection of corticospinal tract compromise in amyotrophic lateral sclerosis with brain MR imaging: relevance of the T1-weighted spin-echo magnetization transfer contrast sequence," *AJNR Am J Neuroradiol,* vol. 25, pp. 1509-1515, 2004.

[53] C. Ellis, et al., "Diffusion tensor MRI assesses corticospinal tract damage in ALS," *Neurology,* vol. 53, pp. 1051-1058, 1999.

[54] M. Cosottini, et al., "Diffusion-tensor MR imaging of corticospinal tract in amyotrophic lateral sclerosis and progressive muscular atrophy," *Radiology,* vol. 237, pp. 258-264, 2005.

[55] C. A. Sage, et al., "Quantitative diffusion tensor imaging in amyotrophic lateral sclerosis," *Neuroimage,* vol. 34, pp. 486-499, 2007.

[56] A. Toosy, et al., "Diffusion tensor imaging detects corticospinal tract involvement at multiple levels in amyotrophic lateral sclerosis," *J Neurol Neurosurg Psychiatry,* vol. 74, pp. 1250-1257, 2003.

[57] Y.-H. Hong, et al., "Diffusion tensor MRI as a diagnostic tool of upper motor neuron involvement in amyotrophic lateral sclerosis," *J Neurol Sci,* vol. 227, pp. 73-78, 2004.

[58] M. S. V. D. Knaap and J. Valk, Magnetic Resonance of Myelination and Myelin Disorders, Springer Science & Business Media, 2005.

[59] T. Gutberlet and J. Katsaras, Lipid Bilayers: Structure and Interactions, Springer Science & Business Media, 2001.

[60] B. S. Brown, Biological Membranes, Biochemical Society, 1996.

[61] F. J. Sharom, "Flipping and Flopping—Lipids on the Move," *IUBMB Life,* vol. 63, p. 736–746, 2011.

[62] A. D. Hamilton, Supramolecular Control of Structure and Reactivity, John Wiley & Sons, 2008.

[63] S. Geyer, et al., Microstructural Parcellation of the Human Cerebral Cortex: From Brodmann's Post-Mortem Map to in Vivo Mapping with High-Field Magnetic Resonance Imaging, Springer Science & Business Media, 2013.

[64] M.-M. E. Mendili, et al., "Multi-parametric spinal cord MRI as potential progression marker in amyotrophic lateral sclerosis," *PLoS One,* vol. 9, p. e95516, 2014.

7. VITA

Jin Gao

Education Background

M.S., Bioengineering

University of Illinois at Chicago, Chicago, IL

Thesis: High b-value Diffusion MRI for Characterizing White Matter Damage

B.S., Food Science and Engineering, July 2011

Inner Mongolia Agricultural University, Hohhot, China

Thesis: Evaluation of Nine Stabilizers in Fruit Grain of Mixed Acid Milk

Research Experience

2016-2017; Graduate Research Assistant

Research Resources Center, University of Illinois at Chicago, Chicago, IL

Honors & Awards

2017   Graduate school travel award & Graduate student council travel award

2011   3rd prize university scholarship & Outstanding student of new employees training of Liquid Milk Department of Inner Mongolia Yili Industrial Group CO., Ltd

2007   2nd prize of the 12th China Adolescents Science & Technology Innovation contest (CASTIC) in Inner Mongolia

2006   3rd prize of China High School Biology Olympiad (CHSBO) in Inner Mongolia

Publications

Lingyan Gao, **Jin Gao**, Linhe Wang. Mechanism for *Spirulina* Live through Winter in Alkaline Lake of Erdos. Journal of Inner Mongolia Agricultural University, 2011(4):84-88

Lingyan Gao, **Jin Gao**, Linhe Wang. Light Adaptability of Tow Strains *Spirulina (Arthrospra) platensis*. Journal of Arid Land Resources and Environment, 2011(11):199-204

Conference Papers

Gao J, Gatto RG, Magin RL, Larson AC, Li W: Preliminary Study of High b-value Diffusion MRI for Characterizing White Matter Damage in A Mouse Model of Amyotrophic Lateral Sclerosis. Proceedings of the 25th Annual Meeting of the ISMRM, p. 7363, Honolulu, Hawaii, 2017.

Li W, **Gao J**, Gordon A, Cai K, Larson AC, Magin RL: High b-value Diffusion-Weighted MRI for Detection of Interscapular Brown Adipose Tissue in Rodent Model. Proceedings of the 25th Annual Meeting of the ISMRM, p. 2997, Honolulu, Hawaii, 2017.

Gatto RG , Li W , Amin M, Colon-Perez L , **Gao J** , Mareci TH, Brady ST, Morfini GA, Magin RL: Spinal Cord MRI Water Diffusion Alterations are Linked to Early Axonal Degeneration in the YFP, G93A-SOD1 mice. Proceedings of the 25th Annual Meeting of the ISMRM, p. 3027, Honolulu, Hawaii, 2017.

Uyanik M, Abern M, Caldwell B, **Gao J**, Karaman M, Mar W, Zhou XJ, Magin RL: Prostate Cancer Classification Using a Stretched Exponential Model of Diffusion. Proceedings of ISMRM workshops on: Breaking the Barrier of Diffusion MRI, Lisbon, Portugal, 2016.